



Consistent closures for Euler-Lagrange models of bi-disperse gas-particle suspensions derived from particle-resolved direct numerical simulations



Federico Municchi*, Stefan Radl

Institute of Process and Particle Engineering, Graz University of Technology, 8010 Graz, Austria

ARTICLE INFO

Article history:

Received 29 November 2016
Received in revised form 21 February 2017
Accepted 31 March 2017
Available online 6 April 2017

Keywords:

Particle-resolved direct numerical simulation
Closure models
Polydisperse
Multiphase flow
Heat transfer
Gas-particle suspensions

ABSTRACT

Particle-Resolved Direct Numerical Simulation (PR-DNS) is employed to simulate momentum and energy transport in bi-disperse gas-solid suspensions by means of a novel hybrid immersed-boundary/fictitious domain (HFD-IB) method. First, we demonstrate the accuracy of the new HFD-IB method against several verification tests. Subsequently, we simulate momentum and energy transfer in bi-disperse suspensions in the limit of high Stokes number, and the predicted flow and temperature fields are used, in conjunction with the open-source parallel data processing library CPPPO (Municchi et al., 2016), to assess the validity of existing closures for momentum and heat transfer in the frame of Particle-Unresolved Euler-Lagrange (PU-EL) models. We propose a correction to the drag force model proposed by Beetstra et al. (2009) which consistently takes into account the pressure contribution to the total fluid-particle interaction force in PU-EL models. Also, we propose a stochastic closure model for the per-particle drag coefficient based on a modified log-normal distribution. Finally, we assess the existence of an analogy between the particle-based drag coefficient and the conditionally-averaged Nusselt number. Indeed, our PR-DNS data indicates that a stochastic closure similar to that for the drag can be used to close the particle-based Nusselt number in dense bidisperse suspensions.

© 2017 Elsevier Ltd. All rights reserved.

1. Introduction

Numerical simulations of large scale particle flows, which are widely encountered in industrial applications, are normally performed using averaged equations of motion. In these descriptions the solid and fluid phases are modeled as interpenetrating continua [3]. These models are normally based on the kinetic theory of granular flows [4] and contain unclosed terms that have to be modeled somehow. In a multi-scale approach [5,6], these models can be derived from more detailed simulations where particles are described as a discrete phase. In particular, in case the trajectory of each particle is tracked and collisions are resolved, one obtains the so-called Computational Fluid Dynamics-Discrete Elements Method (CFD-DEM) that, in case fluid cells are larger than particle diameters, can also be referred to as the Particle-Unresolved Euler-Lagrange approach (PU-EL) [7–13]. However, even PU-EL equations have several unclosed terms, like the interphase transport coefficients, that account for, for example, fluid-particle heat and momentum transfer. Following the multi-scale paradigm in our present contribution, we seek to obtain certain

closures from fully resolved simulations, i.e., where the detailed flow and temperature (or concentration) fields are resolved on a sub-particle level. This latter approach can be denoted as Particle-Resolved Euler-Lagrange (PR-EL), or Particle-Resolved Direct Numerical Simulation (PR-DNS) if turbulence models are used or not, respectively. PR-DNS has already been extensively used to derive closures for the drag coefficient in mono- and bi-disperse suspensions [14,2,15], or for the Nusselt/Sherwood number in mono-disperse suspensions [16–20]. However, almost the totality of this previous work focused on closures for Euler-Euler-based simulations in a coarse scale. Naturally, the question arises of the same closures can be used for PU-EL simulations, and we will demonstrate that indeed this is not the case.

1.1. Upscaling and closure development strategies

A major difference between closures for Euler-Euler and PU-EL models is that the latter require a particle-based description of the interphase transfer processes, while the former (i.e., EE models) require average exchange coefficients. Thus, particle-based models are affected by per-particle fluctuations that arise simply due to the random arrangement of individual particles, and occur even in low-Reynolds number flows. When developing closures for continuum formulations, these quantities, are obtained from averages

* Corresponding author.

E-mail address: fmunicchi@tugraz.at (F. Municchi).

Nomenclature

Abbreviations

CFD	computational fluid dynamics
DEM	discrete element method
DNS	direct numerical simulation
EL	Euler-Lagrange
HFD-IB	hybrid fictitious-domain/immersed-boundary
PR	particle-resolved
PU	particle-unresolved

Greek characters

α	log-normal standard deviation [–]
β	log-normal lower bound [–]
η	particle diameter [–]
γ	correction function
κ	tortuosity [–]
Λ	interphase saturation coefficient [–]
λ_o	characteristic fluid-particle system length [–]
ν	fluid kinematic viscosity [m ² /s]
Ω	computational domain
ω	relaxation factor [–]
ϕ	volume fraction [–]
Φ_m	marker field
Φ_s	sampled field
ρ	phase density [kg/m ³]
σ	scaled standard deviation [–]
Θ	saturation margin [–]
θ	fluid temperature [–]
Q	filter size [–]

Latin characters

\mathbf{f}	total interphase force [–]
\mathbf{u}	velocity field [–]
\mathbf{c}^i	ensemble conditional averaging Kernel [–]
\mathbf{M}	coefficient matrix [–]
\mathbf{U}	discrete binning set [–]
\mathcal{P}	modified log-normal distribution
A	surface [m ²]
A_p	specific exchange surface [1/m]
c_p	fluid thermal capacity [J/kg K]
d	particle diameter [m]
d_{cs}	distance between cell c and particle surface [m]
F	interphase drag coefficient [–]
F_B	Beetstra interphase drag coefficient [–]
F_{corr}	corrected interphase drag coefficient [–]
h	CFD cells per particle diameter [–]
I	indicator function [–]
K	kernel function
k	heat conductivity [W/mK]
N_p	number of particles [–]
Nu	Nusselt number [–]
Nu_{bi}	bi-disperse Nusselt number [–]

p	pressure [–]
Pe	Peclet number [–]
Pe_L	longitudinal Peclet number [–]
Pr	Prandtl number [–]
Q	interface heat transfer rate [–]
r	radial coordinate [m]
Re	Reynolds number [–]
s	HFD-IB interpolation distance [m]
T	temperature [K]
t	temporal coordinate [–]
U_s	superficial velocity [m/s]
v	particle velocity [m/s]
V	CFD cell volume [m ³]
x, y, z	cartesian coordinates [–]

Subscripts/superscripts

(cons)	consistent
\odot	evaluated from the HFD-IB algorithm
$\Phi_{m,j}$	evaluated using discrete marker field at j
<i>Deen, Gunn, Sunn</i>	refers to one of these correlations
F	relative to the drag force
G	global quantity
<i>mix</i>	relative to the homogeneous mixture
Nu	relative to the Nusselt number
*	dimensional quantity
0	reference value
32	mean Sauter quantity
∇p	contribution from pressure gradient
Φ_m	evaluated using marker field
b	bulk quantity
c	property related to CFD cell c
d	contribution from drag
f	property related to fluid phase
g	quantity related to the whole domain (global)
l	imposed value
i	property related to particle number i
k	property related to particles specie k
M	property related to particles with the largest radii
m	property related to particles with the smallest radii
n	quantity at time step n
p	property related to particle phase
$P1, P2$	property interpolated at point $P1$ or $P2$
s	property evaluated at particle surface
<i>sat</i>	value at saturation

Averaging/filtering operators

$\langle(*)\rangle$	ensemble average
$\langle(*)\rangle_\Phi$	ensemble average conditional on Φ
$\overline{(*)}$	volume average
$\langle(*)\rangle$	flux average
$\langle(*)\rangle$	Favre average

within each realization, so that the fluctuations in the particle population are lost and the final standard deviation is calculated based on the ensemble of realizations. On the contrary, closures for PU-EL models are based on the whole studied population and thus, they may require stochastic models to take into account the single particle variability [14,21].

The process of upscaling of fluid quantities that we adopted is known as (spatial) filtering or coarse-graining [22]. The local domain where this operation is performed (in PR-DNS) can be identified with a fluid cell used in PU-EL. In general, closure models derived using this approach have a functional dependence on

the filter size, i.e., the support of the filtering kernel or, in other words, the size of the coarse-grained cell [8]. Moreover, while the velocity field is statistically homogeneous in homogeneous particle configurations, the temperature field is generally inhomogeneous [19,20]. This is in contrast with the assumption of separation of scales required for the development of continuum formulations, e.g., Euler-Euler models, and poses a challenge also in the development of particle-based models such as PU-EL-based models. In the present work we refer to this issue as *saturation*, since this term does reflect the physical process that is behind.

1.2. Immersed-boundary formulations

Studies based on PR-DNS are often performed using immersed-boundary [23] or fictitious domain [24] methods to account for the presence of solid particles, which are often modeled as spheres. A third approach is the "Physalis" method suggested by [25]. This method consists in making use of Lamb's analytical solution for Stokes flow (i.e., using a zero Reynolds number approximation) around a sphere to obtain a high order description of the flow field in the region close to the particle surface. The Physalis method has been successfully applied to moderate Reynolds number suspension flows, and has the key advantages that (i) fluid-particle interaction forces are easily calculated, and that (ii) the numerical error associated with the boundary treatment decreases exponentially. Physalis has been so far applied to flows involving spherical particles only, and it is questionable if the employed zero Reynolds number approximation has an advantage over other boundary approximations for high Reynolds number flows. Generally, in immersed-boundary methods the particle surface is discretized using a set of nodes, spread uniformly on the surface of each immersed boundary, where appropriate forcing terms are computed to impose a Dirichlet (or Neumann) boundary condition. Subsequently, these forcing terms are extrapolated to the surrounding fluid grid, typically by means of a regularized delta function. While these methods are, in general, rather accurate, they may pose a problem of consistency with the underlining transport equations and introduce an additional discretization (i.e., the surface discretization) in the model. On the contrary, in fictitious domain methods, a rigidity constraint is imposed in the fluid region corresponding to the immersed solid body. This constraint is represented as an additional term in the governing equations, so that there are no issues with consistency or convergence. The mathematical formulation normally follows a Lagrangian multiplier based approach [26,27]. Generally, all these kind of direct-forcing methods are focused on imposing the boundary conditions at the immersed surface and/or imposing a rigidity constraint in the fluid region occupied by the immersed body. In the present work, we merge a fictitious domain and an immersed-boundary method to obtain a hybrid method that is consistent, convergent and accurate even on relatively coarse grids. The new method can be used to solve both momentum and scalar (thus energy or mass) transport equations on unstructured grids.

1.3. Effect of size-polydispersity

Polydispersity (i.e., differences in particle size and/or density) is omnipresent in industrial applications and can have various effects. For example, it was shown that the presence of a small amount of fine particles can greatly enhance fluidization [28]. The study of polydisperse suspensions is complicated further by the different inertia of different particle species, which leads to different average velocities between species, and may ultimately lead to segregation. Thus, fixed bed models can be insufficient to correctly picture the momentum exchange processes in fluidized particle beds [29]. In addition, an extensive study of heat transfer in poly-disperse suspensions requires a large computational effort due to the large set of involved parameters (particle diameters and volume fractions of the single species), and the large number of possible configurations that need to be studied to probe enough statistics.

In the past years, polydispersity has been studied in the frame of fluid-particle momentum transfer [2,15]. However, the problem of estimating heat/mass transfer coefficients in polydisperse suspensions has been approached only very recently in the scientific community. Specifically, the rather limited study of Tavassoli et al. [30] (considering Reynolds numbers between 30 and 100)

is the only attempt towards numerical investigation of heat/mass transfer in a random array of size-disperse spheres we are aware of. Even this recent work failed to establish a conclusive model for the distribution of the per-particle Nusselt, simply because not enough statistics could be collected.

1.4. Considerations on numerical simulation of gas-particle suspensions

Gas-particle suspensions are generally characterized by high values of the Stokes number due to the large solid to gas density ratio. This results in the characteristic time of the flow field being much smaller than the characteristic time for the evolution of the particle configuration. In other words, the fluid phase is evolving much faster (eventually reaching a steady state) than the solid phase, allowing the time dependent gas-particle system to be represented as a collection of particle configurations together with steady (or fully developed, if the flow field does not reach a steady state) flow fields. Similar conclusions can be also drawn for the energy transport by noticing that the Prandtl number is close to unity for gases and thus, the temperature field evolves on length and time scales similar to those of the velocity field. In our work we enforce time scale separation to decouple the evolution of the fluid and the particle phase, and therefore we keep the particle cloud fixed while evolving the fluid phase. We do not simulate moving particles. This approach has already been adopted (for the flow field) in the work of Holloway et al. [29]. Furthermore, in fluidized suspensions the effect of particle velocity fluctuations on the drag force is considerably smaller than the effect of the mean fluid-particle slip velocity [31] in the case of low Reynolds number flows. In our work, we speculate that this holds also for moderate (up to 400) Reynolds numbers. With this in mind, we consider static particle distributions (i.e., particles are not allowed to change their position in time) and neglect the effects of relative velocities between different particles.

1.5. Goals and outline

In the present work, we first aim on developing a novel method to account for the presence of immersed bodies in dense particle beds. Second, we apply this method to study transfer of a scalar quantity (i.e., heat and mass) from a random bi-disperse bed of particles. Third, we make use of the open-source library CPPPO [1] to investigate the relationship between (i) closures (for drag coefficient and Nusselt number) developed for continuum models and (ii) particle-based closures that are obtained from coarse-grained fields and individual particle quantities (like interphase heat and drag force). Finally, we aim to explore the effect a bi-disperse particle population has on the Nusselt number to eventually establish an analogy between the coefficients that describe momentum and heat transfer.

Our paper is organized as follows: we give a brief background on the mathematical description and introduce the relevant dimensionless group in Section 2. In Section 3, we describe the phenomenon of saturation to motivate which range of Reynolds and particle concentration should be probed to derive closure laws. This section also contains an analytical model to predict the length and time scales at which saturation occurs. In Section 4 we describe the new hybrid immersed boundary-fictitious domain method, together with some numerical details. We present a set of verification cases for both momentum and heat transfer in Appendix A. In Section 5, we present the results from PR-DNS. In Section 6 we bring our findings into perspective with previous findings in order to highlight the significance of our results.

2. Mathematical formulation

In this work, we formulate the framework that governs flow through the interstices of a bi-disperse particle cloud composed of spherical rigid stationary particles suspended in an incompressible Newtonian fluid. We assume that the fluid density does not depend on the temperature field (i.e., we consider the limit of low temperature differences). Effects of buoyancy and radiation are disregarded as well as viscous heating, so that the momentum equations are decoupled from the energy equation and thus, they can be solved separately. We consider a computational domain Ω subdivided in a purely fluid domain Ω_f , and a fictitious particle domain $\Omega_p = \sum_i \Omega_{p,i}$, where the summation is carried out over all the particles. In our approach, particles are considered as regions where the governing equations are equipped with additional forcing terms to impose a Dirichlet boundary condition at the immersed surfaces.

2.1. Governing equations

In the present work, we use the library CFDEMCoupling® [32] to solve the following dimensionless transport equations:

$$\nabla \cdot \mathbf{u} = 0 \quad (1a)$$

$$\frac{\partial \mathbf{u}}{\partial t} + \nabla \cdot (\mathbf{u}\mathbf{u}) = -\nabla p + Re^{-1} \nabla^2 \mathbf{u} + \mathbf{f}^{\otimes} \quad (1b)$$

$$\frac{\partial \theta}{\partial t} + \nabla \cdot (\mathbf{u}\theta) = Pe^{-1} \nabla^2 \theta + Q^{\otimes} \quad (1c)$$

In the system of Eqs. (1), \mathbf{u} is the dimensionless velocity field, p is the dimensionless pressure field, and θ is the dimensionless temperature field. We also introduced the forcing term \mathbf{f}^{\otimes} used to bend the streamlines to make the flow field consistent with the presence of immersed bodies. The source term Q^{\otimes} represents the contribution from immersed particles in the energy equation. These two terms are detailed in Section 4.

In addition, we introduced the dimensionless group composed by Re , the global Reynolds number, and Pe , the global Peclet number. They are defined as:

$$Re = \frac{U_s d_m}{\nu}, \quad Pe = \frac{\rho_f c_p U_s d_m}{\lambda_f} \quad (2)$$

where U_s is the superficial velocity $U(1 - \phi_p)$, and U is the fluid average velocity, as well as ϕ_p is the total particle volume fraction in the domain. ν is the fluid kinematic viscosity, ρ_f is the fluid density, c_p is the fluid thermal capacity, λ_f is the fluid heat conductivity, and d_m is the diameter of the smallest particle. The choice of using d_m as reference is purely arbitrary, and was found useful to interpret the results of our study as discussed in the next paragraphs. One could also introduce the mean Sauter diameter defined as:

$$d_{32} = \frac{\sum_{k=1}^{n_s} N_k d_k^3}{\sum_{k=1}^{n_s} N_k d_k^2} = \left[\sum_{k=1}^{n_s} \frac{\phi_{p,k}}{\phi_p d_k} \right]^{-1} \quad (3)$$

where n_s is the number of species present in the system, N_k is the number of particles of species k and d_k is the diameter of particles of species k , and $\phi_{p,k}$ is the volume fraction of species k .

We assume that the quantities in Definition 2 do not depend on the temperature or pressure fields, so that the values of Re and Pe can be considered to be constant in space and time. Furthermore, Pe is related to Re by the Prandtl number:

$$Pr = \frac{\rho_f c_p \nu}{\lambda_f} \rightarrow Pe = Re Pr \quad (4)$$

We will limit our present study to the case of $Pr = 1$ so that we can write $Re = Pe$. In this way, the fluid properties (relevant for both momentum and heat exchange) can be fully expressed using just one dimensionless number (Re).

The choice of d_{32} as reference length is consistent with the recent findings in poly-disperse systems [15] and it is a common practice in the field of sprays, in order to quantify an effective drop diameter. However, we made the Navier-Stokes equation dimensionless in such a way that the dimensionless group does not depend on d_{32} . In this way, the values of Re and Pe are not changing with the small to large volume fraction (ϕ_m/ϕ_M) or diameter (d_m/d_M) ratio. In addition, since the particle diameter is made dimensionless with d_m , i.e., $\eta_i = d_i/d_m$, the dimensionless group based on d_m can be straightforwardly converted into dimensionless parameters based on d_{32} if desired.

2.2. Filtering operators for coarse graining

The evaluation of particle based transfer coefficients can be performed in different ways for momentum transfer [2,33,34] and heat transfer [16–18,20]. While previous works aimed to develop such closures for Euler-Euler models, in the present work, we aim to establish correlations for PU-EL models. The main challenge is to provide a description of the velocity and temperature of the fluid phase in regions surrounding each individual particle. This is typically done by averaging the fluid variables around each particle using some kind of Kernel function to apply a statistical weight [3]. We will formally indicate this volume filtering operation as:

$$\overline{(*)} = \iiint_{\Omega} K(\mathbf{x} - \mathbf{x}') (*) d^3 \mathbf{x}' \quad (5)$$

where we denoted the spatial filter Kernel $K(\mathbf{x} - \mathbf{x}')$ as a function in the space coordinate \mathbf{x} . Filtered fluid variables are, then, obtained by applying the Favre averaging operator:

$$\widetilde{(*)} = \frac{\overline{\phi_f (*)}}{\overline{\phi_f}} \quad (6)$$

The choice of a suitable functional form of K plays a major role, and should be mainly driven by the nature of the closure model. In PU-EL simulations, the particle diameter is generally much smaller than the size of the fluid cell and thus, only cell-based values (i.e., averaged over the cell volume) are available to be used as variables in a closure model. This requires the filtering Kernel to have a finite support (e.g., the dimensions of the PU-EL fluid cell), and being able to represent the coarse-graining occurring due to the finite volume formulation of the Eulerian phase in PU-EL simulations. These properties are satisfied by the Top-Hat Kernel:

$$K(\mathbf{x} - \mathbf{x}') = \prod_j \frac{\mathcal{H}\left(\frac{q}{2} - |\mathbf{x}_j - \mathbf{x}'_j|\right)}{q} \quad (7)$$

where \mathcal{H} is the Heaviside step function and q is the dimensionless filter size, defined as q^*/d_p , referring to an equilateral box-shaped filter. In the following, we will refer to the filtered subdomains as coarse grained cells and we will use the notation $\widetilde{(*)}_i$ or $\overline{(*)}_i$ to indicate that filtered quantities are evaluated at \mathbf{x}_i , i.e., at the center of particle i . Using the functional form defined in (7) is equivalent to limit the application of the derived model to (i) structured Cartesian Eulerian grids, and (ii) particles positioned at the exact center of the fluid cell. While the first condition is generally met in well-resolved EL simulations, the second (ii) is generally not, unless particle based values are calculated via linear interpolation from values located in the surrounding cells. Such an interpolation operation is generally cheap (especially for structured grids) when compared to the solu-

tion of large linear systems or the integration of Newton equations for a large number of particles [22]. Hence, linear interpolation is typically considered computationally affordable, and indeed used in almost the totality of all recent works that rely on PU-EL simulations [8].

Next, we introduce the so-called bulk or flux-averaged temperature defined as:

$$\hat{\theta} = \frac{\iint_A \theta \mathbf{u} \cdot d\mathbf{A}}{\iint_A \mathbf{u} \cdot d\mathbf{A}} \quad (8)$$

where \mathbf{A} is a normal vector characterizing a cross sectional area element (i.e., and area element normal to the average flow field). Notice that, unlike other filtering operators, the flux averaging operator removes the dependency with respect to two spatial components (i.e., that in the plane of the element \mathbf{A}). It is clear that closure models that are based on flux-averaged quantities are rather useless, since flux-averaged quantities are generally not available in PU-EL or Two Fluids Models. Despite the fact that this problems has been already addressed in literature [20], all available closure models (except that from [20]) are based on flux averaged quantities, and hence not applicable for PU-EL model.

2.3. Extraction of conditional averages

In the present study particle based quantities are evaluated using the filtering library CPPPO [1]. A conditional average is then performed for each studied parameter removing those sampled values that deviated more than $\pm 2\sigma$ (σ being the standard deviation) from the average. In addition, only averages containing more than 100 individual samples were considered in the study. Following this strategy, particle based quantities (i.e., the samples) are grouped into bins [1]. Within each bin we also constructed the distribution of the sampled values. Thus, we obtain a set of conditionally averaged values and, for each of them, the corresponding distribution of sampled values. This allows us to represent the particle population using a closure for (i) the conditionally-averaged quantities, and (ii) the distribution of per-particle quantities.

Thus, for a generic sampled quantity Φ_s and a marker field Φ_m we define a closed set U_{Φ_m} of equally spaced values of Φ_m such that:

$$U_{\Phi_m} = \{\Phi_{m,j} \in \Phi_m, \quad j \in \mathbb{N}^+ \mid \Phi_{m,j+1} - \Phi_{m,j} = 2\Delta\Phi_m\} \quad (9)$$

here $\Delta\Phi_m$ is the spacing interval. For each particle i , we define the ensemble conditional average kernel function as:

$$C_{\Phi_m,j}^i = \mathcal{H}(\Phi_m^i - \Phi_{m,j} + \Delta\Phi_m) \mathcal{H}(\Phi_m^i - \Phi_{m,j} - \Delta\Phi_m) \quad (10)$$

Which is 1 if the particle marker field value Φ_m^i falls in the discretization interval of $\Phi_{m,j}$ and 0 otherwise. Then, we define the ensemble average of Φ_s conditioned on $\Phi_{m,j}$ as:

$$\langle \Phi_s \rangle_{\Phi_{m,j}} = \frac{\sum_{i=0}^{N_p} \Phi_s^i C_{\Phi_m,j}^i}{\sum_{i=0}^{N_p} C_{\Phi_m,j}^i} \quad (11)$$

Furthermore, we define the conditionally-scaled standard deviation $\sigma_{\Phi_{m,j}}^{\Phi_s}$ as:

$$\sigma_{\Phi_{m,j}}^{\Phi_s} = \frac{1}{\langle \Phi_s \rangle_{\Phi_{m,j}}} \sqrt{\sum_{i=0}^{N_p} (\Phi_s^i - \langle \Phi_s \rangle_{\Phi_{m,j}})^2 \frac{C_{\Phi_m,j}^i}{N_p}} \quad (12)$$

Which is the standard deviation relative to the mean of the values in bin j characterized by marker m scaled with the respective ensemble average value. In the following, we will omit the index j in the notation and we will simply use the notation $\langle * \rangle_{\Phi_m}$ to indicate conditionally averaged values.

3. Saturation phenomena in dense particle beds

In the present work we consider a particle population that is statistically homogeneously distributed in space. Consequently, we expect the velocity field to be statistically homogeneous so that the use of periodic boundary conditions is justified. In contrast, the temperature field will have a statistical biasing due to the advection term $\nabla \cdot (\mathbf{u}\theta)$ in the thermal energy transport equation that makes the resulting field statistically inhomogeneous. This inhomogeneity may lead to the conclusion that periodic boundary conditions do not correctly represent the physics of this process. Nevertheless, periodic boundaries have been previously adopted to study heat and mass transfer in monodisperse liquid-particle suspensions [17] exploiting the fact that, before the fluid approaches the particle temperature everywhere in the domain, there exists a temporal window of constant average Nusselt number (Nu). Unfortunately, the approach of Derksen [17] cannot be applied in the present study since this temporal window is too short to probe statistically significant results. This is simply because of the fact that we consider gas-particle systems for which $Pr \approx 1$. Clearly, the fluid will quickly reach a condition that we refer as *saturation*, and which is closely examined in the rest of this section.

3.1. Definition of the saturation variable

In our present contribution we define the fluid phase to be *saturated* with respect to particle i , or in a global sense, respectively, if:

$$\Theta^i = \frac{\theta_s^i - \tilde{\theta}^i}{\theta_s^i} \leq \Theta_{sat}; \quad \Theta = \frac{\theta_s - \tilde{\theta}}{\theta_s} \leq \Theta_{sat} \quad (13)$$

where θ_s^i is the surface temperature of particle i and $\tilde{\theta}^i$ is the Favre averaged temperature around particle i . We indicate with Θ the saturation margin, and with Θ_{sat} the threshold after which we consider the fluid to be saturated, i.e., close to the thermal equilibrium with the population.

There exist two main reasons why conditions (13) should not occur in the simulated domain.

- i Deviations of local values of θ from $\tilde{\theta}^i$ may induce large fluctuations in the resulting Nusselt number due to the small value of $(\theta_s^i - \tilde{\theta}^i)$. This causes noise in the resulting statistics for the Nusselt number.
- ii If saturation occurs after a short distance (e.g., after $2d_p$), there may be no need for a closure model for the Nusselt number. In fact, it would just be sufficient to set the fluid temperature (assuming that all the particles have the same surface temperature θ_s) to θ_s . Furthermore, the use of a closure in saturated conditions, may lead to numerical instabilities (due to the strong coupling) and thus, to strong oscillations of the temperature field.

In this work, we set the saturation margin Θ_{sat} to 0.05 since we found that local values of θ could experience significant deviations from $\tilde{\theta}^i$.

It should be noted that, unlike Θ^i , Θ is a function of just one spatial coordinate since it depends only on the flux averaged temperature and the (constant) particle surface temperature. However, in case the particle distribution is homogeneous, the particle surface temperature is constant and identical for every particle, and the filter size ϱ is sufficiently large, then also Θ^i is a function of the stream-wise coordinate only. In what follows we take the

z-coordinate as the stream-wise coordinate, i.e., the mean flow direction.

Furthermore, we consider an infinite collection of fluid-particle systems, each of them being a realization of the same macroscopic state (i.e., characterized by identical values for ϕ_p , Pe , θ_s and the particle diameter distribution). We assign to each value of the stream-wise coordinate z all the systems with a particle located at $z^i = z$. This is equivalent to say that, for each value of the coordinate z , it is possible to find a particle configuration such that $\tilde{\theta}(t, z) = \tilde{\theta}(t, z^i)$ with $z^i = z$ (since the temperature field is homogeneous in x and y , we dropped the dependence on these coordinates). Thus, under these considerations, Θ^i can be expressed as a continuous smooth function of the stream-wise coordinate.

In the following, we will make no distinction between Θ^i and Θ since the model we propose can be applied to both the definitions of the saturation margin. Thus, we will refer to the filtered temperature as the coarse-grained temperature, where the coarse graining operator is not explicitly specified, but it is assumed to have commutation properties similar to the Favre averaging operator. Also, we introduce the most relevant Nusselt number closures from literature to subsequently build a simple model that allows us to investigate saturation along the flow direction.

3.2. Available closures for the Nusselt number

For heat transfer in monodisperse particle beds several closures for Nu exist. The most widely used closure is the one proposed by Gunn in 1978 [35]:

$$Nu_{Gunn} = (7 - 10\phi_f + 5\phi_f^2) \left(1 + 0.7Re^{0.2}Pr^{1/3}\right) + (1.33 - 2.4\phi_f + 1.2\phi_f^2) Re^{0.7}Pr^{1/3} \quad (14)$$

An alternative closure was suggested by Deen et al. [16], which used DNS data to refit the closure of Gunn:

$$Nu_{Deen} = (7 - 10\phi_f + 5\phi_f^2) \left(1 + 0.17Re^{0.2}Pr^{1/3}\right) + (1.33 - 2.31\phi_f + 1.16\phi_f^2) Re^{0.7}Pr^{1/3} \quad (15)$$

Another closure obtained from DNS data is the one proposed by Sun et al. [20]:

$$Nu_{Sun} = (-0.46 + 1.77\phi_f + 0.69\phi_f^2) / \phi_f^3 + (1.37 - 2.4\phi_f + 1.2\phi_f^2) Re^{0.7}Pr^{1/3} \quad (16)$$

Notice that we used ϕ_f to indicate $(1 - \phi_p)$ in the above expressions. The last closure is a correction to Eq. (15) for low ϕ_f and will not be used in this work. All these closures where obtained based on a flux averaged temperature and thus, in order to be consistent with coarse-grained models, they must be corrected. Therefore, Sun et al. [20] proposed a correction function that is used to rescale the Nusselt number to obtain $Nu^{(cons)}$ which is consistent with the PU-EL approach:

$$Nu^{(cons)} = Nu_{flux} [1 - 1.6\phi_p(1 - \phi_p) - 3\phi_p(1 - \phi_p)^4 \exp(-Re^{0.4}\phi_p)]^{-1} \quad (17)$$

Here we used Nu_{flux} to indicate the Nusselt number obtained using any of the proposed closures.

3.3. Saturation equation in the case of pure advection

It is possible to derive an analytic expression for the saturation length z_{sat} representing the minimum distance at which condition (13) is satisfied. Let us consider a one dimensional time indepen-

dent model where the local interface heat transfer rate Q balances the convective transport of thermal transport in the bed:

$$Q = U_s \rho_f c_p \frac{dT(z^*)}{dz^*} = h A_p (T_s - T(z^*)) \quad (18)$$

$$h = \frac{Nu k_f}{d_p} \quad (19)$$

Here $T(z^*)$ is a coarse-grained fluid temperature, T_s is the particle surface temperature assumed to be constant, and $A_p = 6\phi_p/d_p$ is the specific exchange surface. Then, Eq. (18) describes the steady advection of the fluid temperature field in the particle bed. We can substitute Eq. (19) into Eq. (18) and integrate to obtain:

$$\ln \left(\frac{T_s - T_{sat}}{T_s - T_0} \right) = - \frac{6Nu\phi_p}{Pe} z_{sat} \quad (20)$$

Noticing that the argument of the logarithm is precisely the saturation margin Θ with $\theta = (T - T_0)/(T_s - T_0)$, the dimensionless saturation length z_{sat} (made dimensionless using the particle diameter, i.e. $z_{sat} d_p = z_{sat}^*$) can be expressed as:

$$z_{sat} = - \frac{\ln(\Theta_{sat})}{\Lambda}; \quad \Lambda = \frac{6\phi_p Nu}{Pe} \quad (21)$$

The above expression gives a measure of the distance (in terms of particle diameters) after which the fluid is nearly in thermal equilibrium with the particle phase. We note in passing that Eq. (18) has been used in other studies to evaluate the mean Nusselt number in mono-disperse particle beds [16,18,36]. Specifically, Eq. (21) can be rearranged such that the value of the Nusselt number is computed from a certain saturation level that occurs at a distance z_{sat} :

$$Nu_{sat} = - \frac{\ln(\Theta_{sat}) Pe}{6\phi_p z_{sat}} \quad (22)$$

Eq. (21) predicts $\lim_{Re \rightarrow 0} z_{sat} = 0$ which would mean that, for very low Reynolds numbers, no closure for the Nusselt number is needed at any scale since the temperature field will quickly saturate. However, this is purely a consequence from the assumption of a steady state: an analysis considering the transients for the fluid temperature yields the following result (respecting the boundary and initial condition $\Theta(0, z) = 1$ and $\Theta(t, 0) = 1$):

$$\Theta(t, z) = e^{-\Lambda z} \mathcal{H}(t - z) + e^{-\Lambda t} (1 - \mathcal{H}(t - z)) \quad (23)$$

where \mathcal{H} is the Heaviside step function. Comparison of Eqs. (20) and (23) reveals that:

$$t_{sat} = z_{sat} = - \frac{\ln(\Theta_{sat})}{\Lambda} \quad (24)$$

Thus, Λ is both the dimensionless time and space relaxation factor, which is homogeneous in the domain. The latter is a fact of our assumption that the particle distribution is homogeneous in the domain. Notice that t_{sat} is a dimensionless time calculated as $t_{sat} = t_{sat}^* U_s / d_p$, being t_{sat}^* a dimensional time.

3.4. Saturation equation with longitudinal dispersion

A more sophisticated model, including an axial dispersion term, can be obtained from direct averaging of the transport equations:

$$\frac{\partial \Theta}{\partial t} + \frac{\partial \Theta}{\partial z} - \frac{1}{Pe_L} \frac{\partial^2 \Theta}{\partial z^2} = -\Lambda \Theta \quad (25)$$

where Pe_L indicates the longitudinal Peclet number defined by the ratio of longitudinal convective and dispersive transport rates. Hence, Pe_L is fundamentally different from Pe , and typically $Pe_L < 2$ and a constant for large Reynolds numbers. When a fluid

is flowing through a bed of inert particles, the measured dispersion is due to the combined effects of molecular diffusion and random fluid motion in the interstices of the bed. The latter phenomenon, also known as pseudo-turbulence, is due to the complex flow pattern induced by the topology of the fluid domain. This results in an anisotropic diffusion tensor since the effects of dispersion are stronger in the direction parallel to the flow field (i.e., in the longitudinal direction) compared to the direction normal to it (i.e., the transverse direction). Several expressions have been suggested for Pe_L , but in this work we follow Delgado [37] and express Pe_L using:

$$\frac{1}{Pe_L} = \frac{1}{\kappa Pe} + \frac{Pe}{5} (1-p)^2 + \frac{Pe^2}{25} p(1-p)^3 \left(e^{-\frac{5}{p(1-p)Pe}} - 1 \right) \quad (26)$$

$$p = \frac{0.48}{Pr^{0.15}} + \left(\frac{1}{2} - \frac{0.48}{Pr^{0.15}} \right) e^{\frac{0.75Pr}{Pe}} \quad (27)$$

where κ is the tortuosity (which equals $\sqrt{2}$ for spheres). One key feature of Pe_L is that for $Pe > 1$ the relation $Pe_L \ll Pe$ always holds.

Eq. (25) can be solved using the same boundary and initial conditions used for (23), plus an additional one due to the second order term. Specifically, we choose $\Theta(t, \infty) = 0$, which means that the two phases are in thermal equilibrium far downstream of the inlet. This set of boundary conditions ultimately leads to:

$$\Theta(t, z) = e^{-\Lambda t} + z e^{\frac{Pe_L}{2}} \int_0^t \frac{1 - e^{-\Lambda(t-\tau)}}{2 \sqrt{\frac{\pi \tau^3}{Pe_L}}} e^{\left[\frac{z^2 Pe_L}{4\tau} - \left(\frac{Pe_L}{4} + \Lambda \right) \tau \right]} d\tau \quad (28)$$

Unfortunately, the analysis of the transient response is complicated by the convolution term. However, a useful solution can be obtained for the steady-state situation which is much easier to manipulate:

$$\Theta(z) = e^{-z/\lambda_o} \quad (29)$$

$$\lambda_o = \frac{1}{\sqrt{\frac{Pe_L^2}{4} + Pe_L \Lambda - \frac{Pe_L}{2}}} \quad (30)$$

where we introduced the characteristic fluid-particle system length λ_o which represents the distance at which a perturbation in the Θ field is reduced by a factor e in a fluid-particle system with a homogeneous distribution of isothermal particles.

Following Eq. (29), the saturation length becomes:

$$Z_{sat} = -\ln(\Theta_{sat}) \lambda_o \quad (31)$$

It is easy to show that Eq. (31) returns Eq. (21) in the limit of infinite Pe_L (i.e., in the absence of longitudinal dispersion) for any finite value of Pe . Also, we note that λ_o is always larger than the corresponding length scale $1/\Lambda$ in a system without dispersion. Thus, longitudinal dispersion alleviates the saturation problem to some degree. Next, it can be shown that in the limit of $Pe \rightarrow 0$ Eq. (31) gives:

$$Z_{sat} = -\frac{\ln(\Theta_{sat})}{\sqrt{6\kappa\phi_p Nu|_{Pe=0}}} \quad (32)$$

A major difference between Eqs. (28) and (23), is that when dispersion is considered, the steady state solution is only reached asymptotically. In fact, no Heaviside function appears in Eq. (28) and thus, the time t_{sat} can only be evaluated for $z > Z_{sat}$ instead of $z = Z_{sat}$. However, it is still true that, after a time t_{sat} is elapsed, we obtain $\Theta(t, z) > \Theta_{sat}(t_{sat}, Z_{sat})$ in $z > Z_{sat}$. Thus, also in this case after a dimensionless time t_{sat} has passed, the state of pseudo equilibrium is reached everywhere. In addition, numerical evaluation of Eq. (28) shows that:

$$t_{sat} < Z_{sat} \quad (33)$$

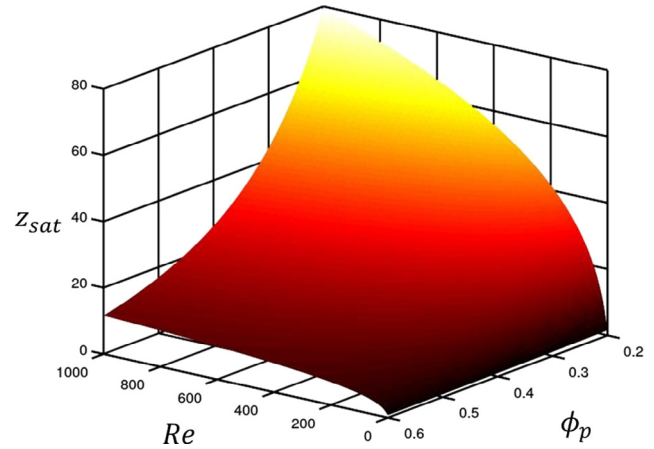


Fig. 1. Map showing the value of Z_{sat} as a function of Re and ϕ_p . We used Eq. (15) to evaluate the Nusselt number, consider longitudinal dispersion, as well as assume $Pr = 1$.

Which means that for any position z downstream from Z_{sat} the state of pseudo-equilibrium is reached (slightly) faster than in the dispersion-free case. We also observed that t_{sat} increases almost linearly with Z_{sat} . It is then appropriate to state that t_{sat} has approximately the same value as Z_{sat} and thus the (dimensionless) heat and mass transfer space and time scales are of the same order for this class of fluid-particle systems.

Fig. 1 summarizes typical values for Z_{sat} , and illustrates that the saturation length can be rather small, even at high values of the Reynolds number and in dense beds. Thus, we observe for $\phi_p = 0.5$ that Z_{sat} is always smaller than 20 (the saturation length was made dimensionless with the particle diameter) over the full range of Reynolds numbers, i.e., in such situations the fluid domain will saturate very quickly.

As shown in Fig. 2, the above model with dispersion is able to reasonably predict the value of Θ and thus, the coarse-grained temperature in the particle bed. The overall agreement is satisfactory, especially considering that the comparison of Eq. (25) is carried out against calculations from ensemble averaged PR-DNS data. Also, Deen et al.'s correlation approximates our PR-DNS reasonably well (see Section 5.4).

4. Numerical formulation

The software employed in the present work, i.e., OpenFOAM®, uses co-located variables (i.e., all variables are defined at cell centers), and relies on a finite volume method for arbitrarily-shaped cells. The system of equations is solved in a segregated manner, i.e., it is solved within an iterative sequence. In the present work we use a structured Cartesian mesh where spherical particles are represented by forcing terms in the matrix equations. This greatly reduces the efforts for generating the numerical grid (which is required for more standard body-fitted mesh approaches). Also, the presented approach ensures that no errors arise due to the grid cell topology, making the overall accuracy estimation easier. Local mesh refinement at particle surfaces is performed dividing each hexahedral cell into eight smaller hexahedral cells, and imposing a determinant equal to one on each new cell.

4.1. Hybrid fictitious-domain/immersed-boundary method

In a discrete computational domain using non-conformal mesh elements the topology of the fluid-solid interface cannot be accurately represented. This lack of topological accuracy is affecting

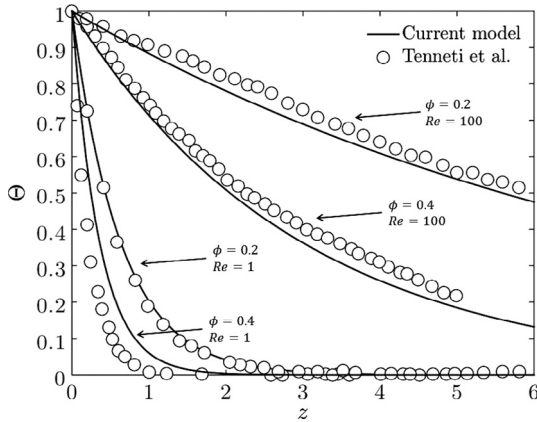


Fig. 2. Θ versus dimensionless streamwise coordinate z to compare DNS data from Tenneti et al. [19] with predictions from the one-dimensional convection-dispersion equation, i.e., Eq. (31) using the closure for the Nusselt number from Deen et al. [16].

the particle fluid exchange processes and requires an analytic representation of the immersed boundary alongside with the appropriate forcing inside the immersed body. The HFD-IB (Hybrid Fictitious Domain Immersed Boundary) solver allows to represent the immersed surface, and to account for the presence of the immersed body. The idea is to combine the convergence properties of a Lagrangian multiplier fictitious domain method [26,27,38–40] with an immersed boundary method [23,41] that acts like a convergence accelerator.

The fictitious-domain/immersed-boundary method combines some elements from both formulations in order to:

- Provide an accurate representation of the particle topology in the discretized domain and, thus applying the corresponding boundary condition at the particle surface (which in general does not coincide with any cell node or cell center).
- Being convergent (i.e., recover the original equations when the grid size tends to zero).
- Ensure consistency of the imposed forcing/source terms with the interphase exchange process.

The latter assertion means that integrating the forcing/source term over the particle volume should give the interphase exchange rate. To be specific, the dimensionless force acting on a particle due to the fluid phase and the total dimensionless heat transferred from a particle i to the surrounding fluid should be respectively expressed by:

$$\mathbf{f}_i(t) = - \int_{\Omega_i^i} \mathbf{f}^{\circ}(\mathbf{x}, t) d^3 \mathbf{x} \quad (34)$$

$$Q_i(t) = \int_{\Omega_i^i} Q^{\circ}(\mathbf{x}, t) d^3 \mathbf{x} \quad (35)$$

Eqs. (34) and (35) represent the mapping of the interface coupling terms from the Eulerian fluid domain to the Lagrangian particle cloud. In order for Eq. (35) to hold, it has to be ensured that no heat transfer occurs inside the immersed body, i.e., the immersed body should be represented by a region of constant fluid temperature θ_i while an appropriate surface temperature θ_s should be imposed in order to satisfy the Dirichlet boundary condition. Eq. (34) would require a similar condition (i.e., imposed fluid velocity inside the rigid body). However, the required forcing would trigger a flow circulation at the particle surface due to continuity (i.e., the fluid would flow outside the particle). This would result in the hot

fluid inside the particle to be artificially transported to the particle surface creating an additional inter-phase heat flux not accounted in Eq. (35). If the immersed body rigidity is not imposed, the forcing term (which would be non-zero only at the particle boundary) would trigger a flow internal to the particle which would dissipate energy by friction, thus overestimating the inter-phase momentum transfer. In fact, the fluid inside the immersed body should be frictionless [42]. In order to avoid this problem, the HFD-IB forces the particle surface only, but keeps track of the additional forcing that would be needed in order to stop the flow inside the immersed body. Eq. (34) is then substituted by:

$$\mathbf{f}_i(t) = - \int_{\partial\Omega_i^i} \mathbf{f}^{\circ}(\mathbf{x}, t) d^3 \mathbf{x} + \int_{\Omega_i^i - \partial\Omega_i^i} \Delta \mathbf{f}^{\circ}(\mathbf{x}, t) d^3 \mathbf{x} \quad (36)$$

where $\Delta \mathbf{f}^{\circ}(\mathbf{x}, t) = \mathbf{f}^{\circ}(\mathbf{x}, t) - \mathbf{f}^{\circ}(\mathbf{x}, t - \Delta t)$ is the change in the forcing term required to impose a fixed value of the velocity field inside the rigid body. Notice that $\partial\Omega_i^i$ is the discretized particle surface (i.e., cells at the particle surface) and thus the second term on the RHS of Eq. (36) represents the forcing only in the interior of particle i . This ansatz allows us to effectively remove the transfer of momentum to the inside of the particles, and Eq. (36) now represents only the fluid-particle interaction force between the particles and the main flow outside of the particle domain. We note that $\Delta \mathbf{f}^{\circ}$ does only contribute marginally to the total forcing (it is on the order of 0.01%), especially in case the flow and temperature fields are stationary. Also, we note that in other methods [43] the rigidity condition is still imposed inside the solid domain, possibly resulting in unwanted fluxes through the boundary.

4.1.1. Boundary layer reconstruction approach

An accurate imposition of the Dirichlet boundary condition at the particle surface is performed through a second order boundary layer reconstruction procedure. The present approach can be regarded as a generalized second order version of other approaches found in literature [44–46], since the method we propose is independent of the interpolation scheme used. In fact, our proposed method works with all interpolation schemes available in our software toolkit (i.e., OpenFOAM®). In our boundary layer reconstruction approach, field values in cells that are cut by the particle surface (denoted as “surface cells” below) are forced to assume certain values (i.e., \mathbf{u}_i and θ_i). These values are generally different from the corresponding values located at the particle surface (\mathbf{u}_s and θ_s). We now consider an interpolation stencil round each surface cell, and use a second order polynomial to reconstruct the fluid phase properties along the radial direction (see Fig. 3). The interpolation points are spaced by the surface distance s defined as:

$$s = \sqrt[3]{3V_c} \quad (37)$$

where V_c is the volume of the surface cells. It is clear that s represents the diagonal of the cubic surface cell, so that the interpolation points will always be located in different cells when the numerical grid is sufficiently regular close to the particle surface, i.e. if the cell shape is approximately cubic and if there is no significant shape or size difference between two neighboring cells. The surface cell value to be imposed is then evaluated from (for simplicity, we illustrate the interpolation procedure only for θ , similarly this idea can be applied to the velocity field):

$$\theta_{c,l} = \frac{\theta_{p2} - 2\theta_{p1} + \theta_s}{2s^2} d_{cs}^2 + \frac{4\theta_{p1} - \theta_{p2} - 3\theta_s}{2s} d_{cs} + \theta_s \quad (38)$$

where θ_s is the particle surface value, θ_{p1} is the interpolated value of θ at point $P1$, θ_{p2} is the interpolated value of θ at point $P2$, and d_{cs} is the distance between the surface cell center and the particle surface.

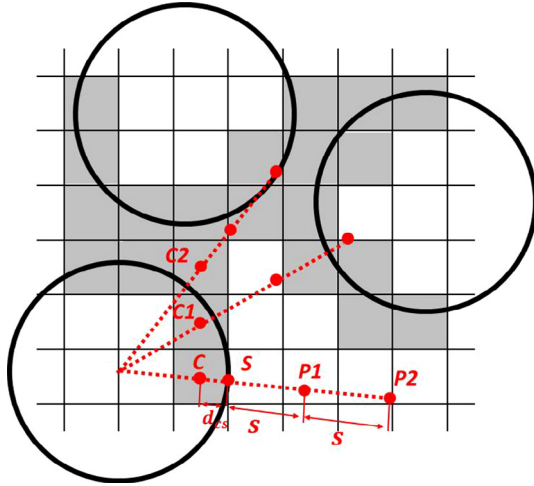


Fig. 3. Representation of immersed surfaces on a Cartesian grid (here shown in two dimensions for the sake of simplicity). Circles represent the immersed particle surfaces, while surface cells are colored in gray. Cell value at C is evaluated based on S, P1, and P2 using a second order polynomial. Conversely, C1 and C2 are evaluated using a first and zero order approximation, respectively, due to insufficient reconstruction points in the interpolation stencil.

It is clear that, in order for the interpolated field values to have a physical meaning, there should be no other particle within the interpolation stencil. While this condition is almost true for very dilute suspensions and for very fine (compared to the particle diameter) grids, it cannot be guaranteed for a general situation. In order to overcome this problem, our proposed method adjust its order (and thus, its interpolation stencil) based on the value of ϕ in the cells close to the interpolation points. In fact, those cells whose center is inside a particle (i.e., $\phi > 0.5$) should not contribute to the boundary layer reconstruction since their value is merely used to satisfy the Dirichlet boundary condition for a certain particle surface cell. Since the interpolation itself may require a (possibly different) computational stencil, we discard an interpolation point if one of its three closest cells has a value of ϕ higher than 0.5. An example is given in Fig. 3. Whenever an interpolation point is discarded, the order of the boundary layer reconstruction is automatically decreased. That is, if only the furthest interpolation point is discarded the interpolation is carried out using:

$$\theta_{c,l} = \frac{\theta_{p1} - \theta_s}{s} d_{cs} + \theta_s \quad (39)$$

However, if the closest interpolation point is discarded, a zero order approximation is used:

$$\theta_{c,l} = \phi \theta_s + (1 - \phi) \theta_c \quad (40)$$

Notice that in Eq. (40) the new cell value is calculated using the field ϕ as a penalty factor like in the standard fictitious domain methods. Thus, a pure fictitious domain approach can be seen as a zero order HFD-IB. In addition, it is clear that in this method the immersed surface is discretized together with the numerical grid (i.e. no separate Lagrangian representation of the particle surface) and in the limit of zero grid spacing Δx we obtain:

$$\lim_{\Delta x \rightarrow 0} s = 0 \quad \rightarrow \quad \theta_{c,l} = \theta_s \quad (41)$$

Thus, we impose the exact Dirichlet boundary condition and, in the limit, the method is formally equivalent to a Lagrangian multiplier fictitious domain.

4.1.2. Point interpolation methods

Since the HFD-IB is implemented in the OpenFOAM® framework, there are several interpolation schemes that can be used for the reconstruction. We tested all of them, and concluded that the best accuracy is achieved using the *cellPointFace* scheme which calculates the interpolated value as an average of closest vertex, face, and cell center values weighted with the inverse distance.

4.1.3. Fluid forcing and source term formulation

The forcing term for the momentum equation is formulated following the work of Blais et al. [47]. This approach is also similar to the one described in [27], and uses a parameter $\omega_f \in [0, 1]$ to adjust the implicitness of the force correction.

$$\mathbf{f}^{\otimes, n} = I_s^n \left(\mathbf{f}^{\otimes, n-1} + \omega_f \frac{\mathbf{u}_i^n - \mathbf{u}^n}{\Delta t} \right) \quad (42)$$

where the superscripts n and $n - 1$ refer to the current and previous step (referring to the stepping in the momentum corrector loop) respectively. Δt is the time step and I_s is a function that is 1 in particle surface cells and zero elsewhere. Our algorithm uses a PISO-IB loop, same as in [47], to correct the forcing and pressure field allowing to fulfill the continuity equation, and to enforce now flow through the immersed boundaries.

The source term for the scalar transport is formulated in a slightly different way since no correction loop is required. This is because the scalar and momentum equations are decoupled and the scalar transport equation is solved after the momentum corrector (i.e., using the solenoidal velocity field). Thus, we next consider the linear system arising from the discretization of the scalar transport equation. Each linear equation can be represented by:

$$M_{ll} \theta_l = Q_l^{\otimes} - \sum_m M_{ml} \theta_m \quad (43)$$

where M is the coefficient matrix of the discretized system of equations and the two subscripts refer to the row and column index. Terms in M are evaluated from the OpenFOAM® matrix assembler following the discretization schemes defined in Section 4.2. The local interphase heat exchange rate at the step $n + 1$ is calculated from:

$$Q_l^{\otimes, n+1} = I_p \left(M_{ll} \theta_{l,l}^n + \sum_m M_{ml} \theta_m^n \right) \quad (44)$$

Being I_p a function that is 1 if the cell belongs to the particle (surface or interior cells) and zero elsewhere. When Eq. (44) is substituted into Eq. (43), wherever $I_p = 1$, we obtain:

$$\theta_{l,l}^{n+1} = \theta_{l,l}^n \quad (45)$$

Thus, the exact imposition of the interpolated value. Notice that, however, update of the imposed scalar field $\theta_{l,l}$ is performed explicitly.

4.2. Numerical solution

The momentum and energy equations were discretized in space using central difference schemes, and a backward scheme was adopted for discretization in time. The pressure coupling was carried out by means of a PISO algorithm that also corrects the immersed boundary forcing [47]. All the discretization methods we adopted were second order accurate. The Poisson equation for the pressure field was solved using a diagonal incomplete-Cholesky preconditioned conjugate gradient method. The momentum and scalar transport equations were solved using a diagonal incomplete lower-upper preconditioned bi-conjugate gradient. In order to preserve the natural evolution of the simulated fields, no relaxation factors were used for equations or fields, i.e., the simu-

lations were performed fully transient. The transient nature of our simulations is fundamentally due to the formulation of the forcing term in the Navier-Stokes equations (Eq. (42)), but we interrupted our simulations when both the velocity and temperature fields reach a steady state conditions, i.e. when the integral carried over all the computational domain of \mathbf{f}^* and Q^* is not changing significantly with time. Specifically, a simulation ends if, for the last 25% of the simulated time, (i) the average absolute value of the fluctuations was less than 0.5% and (ii) the sum of the fluctuations was zero, i.e. if the integrals are weakly fluctuating but not evolving. It should be noticed that condition (ii) is always satisfied in our computational domains after a sufficiently long time due to the heat sink that balances the interphase heat exchange and the imposed pressure gradient that balances the interphase momentum exchange. The algorithm was tested and verified under several operating conditions against data found in literature. Results from some of these tests are presented in the Appendix.

4.3. Computational setup

We make use of a fully periodic rectangular cuboid domain filled with a bi-dispersed particle population (Fig. 4). The particle configuration is generated using LIGGGHTS[®] [32] to generate a homogeneous distribution before the fluid simulation is started. We studied several cases for different values of the overall particle volume fraction ϕ and particle diameters d_1 and d_2 .

The fluid flow is driven by imposing a pressure difference between two opposite faces of the domain in the x_1 direction (which we will refer as the streamwise direction). This pressure drop is adjusted such that the fluid superficial velocity $U(1 - \phi)$ remains constant.

We included a sink term in Eq. (1c) in order to enforce a predefined mean fluid temperature θ_{bulk} at the inlet (see Fig. 4). This is done in order to prevent saturation of the fluid phase with the transferred scalar field. Notice that our approach is similar to the one of Tenneti et al. [19] with the sole difference that we do not modify the periodic boundary, but we rescale the scalar in the first two cell layers downstream the inlet. This approach allows to study flow and scalar fields in fully developed conditions, i.e. without the influence of inlet or outlet boundary conditions. In this sense, our approach is significantly different from that of Tavassoli

et al. [30] who used Dirichlet and Neumann boundary conditions for the inlet and outlet respectively.

It is clear that filtering the temperature field across streamwise periodic boundaries produces unphysical results due to the jump in the temperature field. This means that particle-based quantities can only be studied at a certain distance away from the streamwise periodic boundaries (see Fig. 4). Thus, filtering requires relatively long computational domains, which increases the risk of fluid becoming saturated in the studied region. Hence, in order to prevent saturation phenomena, the Reynolds number must be sufficiently high to ensure a significant mean temperature gradient between fluid and particles over the full bed length.

5. Simulation of bi-dispersed suspensions

5.1. Numerical settings

We restricted our study to the parameters shown in Table 1 and to a domain size of $5d_m \times 5d_m \times 10d_m$ according to the available computational resources. The investigated values of the Reynolds number are relatively high when compared to previous studies [18,16,20] so that the heat exchange does not lead to unwanted excessive fluid phase saturation that would deteriorate the statistics of the Nusselt number. Unfortunately, high Reynolds number flow simulations are demanding in terms of mesh resolution, and hence require a fine computational mesh. Therefore, we performed a grid sensitivity analysis on the most critical cases to assess a suitable grid resolution and the associated error. We concluded that this grid resolution is $h = \Delta x/d_m = 50$ at the particle surface, while a larger grid spacing of $h = 25$ between the particles (i.e., in regions in which velocity gradients are less steep) is adequate. Specifically, in the present study we adopted a base mesh with $h = 25$, and then used mesh refinement at the particle surface. The refinement consisted of splitting a coarse cubic cell of the base mesh into eight equally-sized cubic subcells. The error due to the use of mesh refinement (compared to using a uniformly fine grid with $h = 50$) was found to be less than 1%. Overall, we estimated the maximum error connected to the evaluation of the Nusselt number (with respect to a grid independent solution) to be approximately 20%, similar to the error estimated in previous works [20].

5.2. Drag coefficient in bidisperse particle beds

In the present work, we imposed a constant average superficial fluid velocity in the simulated domain by means of a global pressure gradient. As a consequence, the total force acting on a particle \mathbf{f}_i is next defined as the sum of the fluid drag force \mathbf{f}_i^d and a contribution from a mean pressure gradient $\mathbf{f}_i^{\nabla p}$ that builds up in the bed of particles. Thus, we write:

$$\mathbf{f}_i = \mathbf{f}_i^d + \mathbf{f}_i^{\nabla p} \quad (46)$$

In simulations using a PU-EL model, the contribution from the mean pressure gradient can be explicitly computed based on a known (resolved, but spatially average) pressure field \tilde{p} . We are therefore interested in the remaining force contribution, i.e., the drag contribution in Eq. (46), for which a closure must be provided in PU-EL models. Thus, in what follows we filter the pressure gradient field ∇p based on our PR-DNS data, and define the per-particle drag force as follows:

$$\mathbf{f}_i^d = \mathbf{f}_i - \frac{\pi}{6} d_i^3 \tilde{\nabla p}_i \quad (47)$$

We stress that this definition is the most natural choice, since $\tilde{\nabla p}_i$ is the pressure gradient that would be available in a PU-EL simulation where the CFD cells are of the same size as the filter size.

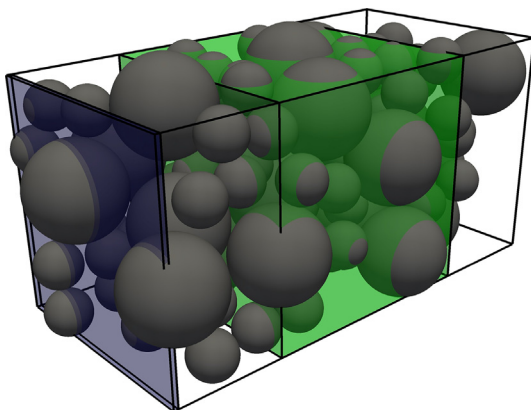


Fig. 4. Computational domain for the dense bi-disperse bed ($\phi = 0.5$, $d_2/d_1 = 2$). A mean flow field is imposed, which is aligned with the longest edge and so, the temperature inhomogeneity develops in that direction. The region where particle-based quantities can be studied for values of ρ up to 5 (thus at $2.5d_m$ from the streamwise boundaries) is colored in green. A heat sink is positioned at the domain entrance (colored in blue) to prevent saturation of the fluid with the transferred scalar. (For interpretation of the references to color in this figure legend, the reader is referred to the web version of this article.)

Table 1

Numerical parameters used in the current study. η_M is the dimensionless particle diameter ratio, ϕ_m/ϕ_M is the ratio of the small particle volume fraction over that of the large particles, N_{pM} is the number of large particles, and N_{pm} is the number of small particles.

ϕ_p	η_M	ϕ_m/ϕ_M	Pe	N_{pM}	N_{pm}
0.20	1.2	0.5	100,250,400	37	33
0.35	1.2	0.5	100,250,400	64	55
0.50	1.2	0.5	100,250,400	92	79
0.20	1.2	1.0	100,250,400	28	48
0.35	1.2	1.0	100,250,400	48	83
0.50	1.2	1.0	100,250,400	69	119
0.20	1.2	2.0	100,250,400	18	62
0.35	1.2	2.0	100,250,400	32	111
0.50	1.2	2.0	100,250,400	46	159
0.20	1.6	0.5	100,250,400	16	33
0.35	1.6	0.5	100,250,400	27	57
0.50	1.6	0.5	100,250,400	39	82
0.20	1.6	1.0	100,250,400	12	49
0.35	1.6	1.0	100,250,400	20	82
0.50	1.6	1.0	100,250,400	29	119
0.20	1.6	2.0	100,250,400	8	66
0.35	1.6	2.0	100,250,400	14	115
0.50	1.6	2.0	100,250,400	19	156
0.20	2.0	0.5	100,250,400	8	32
0.35	2.0	0.5	100,250,400	14	56
0.50	2.0	0.5	100,250,400	20	80
0.20	2.0	1.0	100,250,400	6	48
0.35	2.0	1.0	100,250,400	10	80
0.50	2.0	1.0	100,250,400	15	120
0.20	2.0	2.0	100,250,400	4	64
0.35	2.0	2.0	100,250,400	7	112
0.50	2.0	2.0	100,250,400	10	160

We note that this definition of the drag force is different from that typically used in Euler-Euler simulations, since in the latter the global mean pressure gradient (experienced by all particles) is used to define the drag [15].

The drag force parallel to the main flow direction $f_i^{d\parallel}$ is then made dimensionless (or scaled) with the corresponding Stokes drag force to obtain (dimensional and dimensionless form):

$$F_i = \frac{f_i^{*,d\parallel}}{3\pi d_i \rho_f \nu (1 - \bar{\phi}_i) \tilde{u}_i^{*,\parallel}} = \frac{f_i^{d\parallel} Re}{3\pi \eta_i (1 - \bar{\phi}_i) \tilde{u}_i^{\parallel}} \quad (48)$$

Notice that, since we used filtered quantities (i.e., \tilde{u}_i^{\parallel} and $\bar{\phi}_i$), the dimensionless drag force calculated using Eq. (48) does not respect the usual limit $\lim_{\phi, Re \rightarrow 0} F_i = 1$ for a finite value of ϕ . This happens because F_i is particle-based, and not an ensemble average. Thus, it is possible that the $f_i^{d\parallel} = 0$ while $\tilde{u}_i^{\parallel} \neq 0$ (e.g., in case a particle does not experience a net drag force due to blockage from other particles, but the filtered velocity is non-zero). Our simulation results suggest that this results in F_i to be lower-bounded to 0 instead of 1.

A comparison of the ensemble-averaged drag force evaluated from our PR-DNS data by using Eqs. (46) and (47) with the closure provided by Beetstra et al. [2] is presented in Fig. 5. Beetstra's closure for drag force in bi-dispersed suspensions can be written as a correction to the mono-dispersed drag force $F_{i,B}^m(Re_i, \bar{\phi}_i)$, i.e.,

$$F_{i,B} = \left[(1 - \bar{\phi}_i) y_i + \bar{\phi}_i y_i^2 + 0.064 (1 - \bar{\phi}_i)^3 \right] F_{i,B}^m(Re_i, \bar{\phi}_i) \quad (49)$$

$$F_{i,B}^m(Re_i, \bar{\phi}_i) = \frac{10\bar{\phi}_i}{(1 - \bar{\phi}_i)^2} + (1 - \bar{\phi}_i)^2 \left(1 + 1.5\bar{\phi}_i^{\frac{1}{2}} \right) + \frac{0.413 Re_i}{24(1 - \bar{\phi}_i)^2} \left[\frac{(1 - \bar{\phi}_i)^{-1} + 3\bar{\phi}_i(1 - \bar{\phi}_i) + 8.4 Re_i^{-0.343}}{1 + 10^{3\bar{\phi}_i} Re_i^{-(1+4\bar{\phi}_i)/2}} \right] \quad (50)$$

$$Re_i = Re(1 - \bar{\phi}_i) |\tilde{u}_i| \eta_i; \quad y_i = \frac{d_i}{d_{32}} \quad (51)$$

Notice that, in order to calculate $F_{i,B}$, we only used values obtained by filtering within a box with dimensionless size q . Furthermore, we note that Re_i does not differ significantly if defined using the parallel (to the main flow) filtered velocity \tilde{u}_i^{\parallel} , or the modulus $|\tilde{u}_i|$.

Panel a of Fig. 5 reveals, on average, a significant deviation from the closure proposed in the work of Beetstra et al. Such a deviation can be explained examining the approach they used to calculate the pressure contribution to the drag force. Specifically, two facts need to be considered:

- i Since the particle distribution is homogeneous, it is possible to define a global pressure gradient which corresponds to the pressure gradient required to drive the fluid flow through the interstices between particles in an infinitely large bed (or, in other words, through the equivalent porous medium). Therefore, following our method the local filtered pressure gradient should approach the global one in the limit $q \rightarrow \infty$. However, as visible from panel a of Fig. 5, our results are insensitive of q already for $q > 3$. This was also confirmed by checking the mean difference between the global pressure gradient (calculated as the pressure gradient required to drive the flow field through the whole computational domain) and that experienced by individual particles (data not shown; more details are, however, provided in Appendix B). Thus, the use of the local pressure gradient in place of the global one, contributed significantly only for $q < 3$. A tentative physical explanation is that, for the moderate Reynolds numbers studied here, the fluctuations of the pressure due to acceleration and deceleration of the fluid become already significant, and are noticeable only for small filter sizes. The approach of Beetstra et al. does not account for filter sizes, and only the global pressure gradient was considered (how-

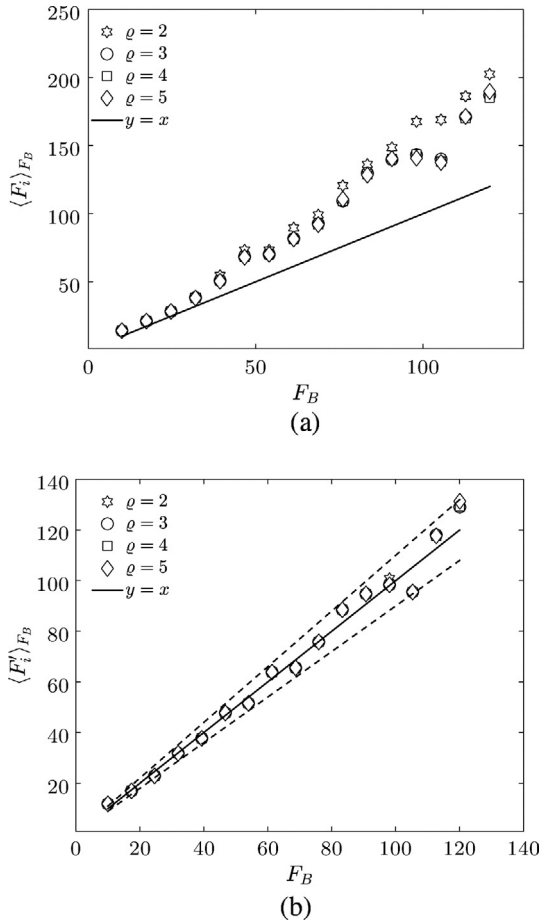


Fig. 5. Parity plot comparing the normalized drag force from the current simulations with values predicted by Beetstra et al. Dashed lines represent 10% deviation from the closure of Beetstra. In panel (a), $\langle F_i^d \rangle_{F_B}$ was calculated using Eqs. (46) and (47). In panel (b) the drag force $\langle F_i \rangle_{F_B}$ accounts for the pressure gradient contribution using Eq. (52) same as in the work of Beetstra et al.

ever, as discussed before, it was not subtracted explicitly). This contributes (in part) to the discrepancy observed in Fig. 5a.

- ii Deviations from the correlation of Beetstra et al. for values of $\varrho > 3$ can be explained by considering that the approach used in their work to remove the pressure contribution from the total drag force cannot be applied to polydisperse suspensions or particle-based forces. In fact, we show in Appendix B that implicit accounting of this pressure gradient term can only be performed on globally averaged quantities (i.e., ensemble averages over all particles and species). In Appendix B we also show that our data is in good agreement with the correct theoretical predictions for the mean pressure gradient contribution. On the contrary, this term is overestimated in the work of Beetstra et al. and thus, they obtain a smaller drag force.

In Appendix B we show that, under particular assumptions, the ensemble average drag force exerted on all particles can be expressed as the ensemble average total fluid-particle force multiplied by $(1 - \phi_p)$. In the work of Beetstra et al., the pressure contribution to the bi-disperse drag force was (incorrectly) accounted for by exploiting this relation, i.e., they used:

$$F_k(\phi, Re) = -(1 - \phi_p) \frac{\langle F_{g \rightarrow s} \rangle}{3\pi\mu d_k v} \quad (52)$$

Being $\langle F_{g \rightarrow s} \rangle$ the ensemble averaged fluid-particle force (acting on particles of specie k) and v the particle velocity. We find that our results are in good agreement (within 10%) if Eq. (52) was used to account for the pressure gradient force $\mathbf{f}^{\nabla p}$ and when using $\bar{\phi}_i$ instead of ϕ_p (see panel b of Fig. 5). In other words, our data suggests that the average pressure gradient seen by the particles is different (i.e., smaller, since we compute higher drag coefficients) from the average pressure gradient in the whole particle bed. A tentative physical explanation is that for the relatively high Reynolds numbers studied here, the fluctuations of the pressure due to acceleration and deceleration of the fluid become already significant. We speculate that this leads to the observed differences visible in panels a and b of Fig. 5). Clearly, the correct way to account for the pressure contribution in PU-EL models is provided by Eq. (47), since each particle is supposed to experience a different local pressure gradient. In addition, the value of $\bar{\nabla} p_i$ is directly available in PU-EL simulations and thus, it can be directly used to compute the per-particle pressure gradient force. Hence, we need to refit the expression suggested by Beetstra et al. to provide a drag closure for PU-EL models. Panel b in Fig. 5 suggest that a simple correction can be applied to F_{iB} to obtain such a PU-EL-consistent drag force closure. Specifically, we propose:

$$F_{i,corr} = -0.122 + 1.18F_{iB} + 0.00352F_{iB}^2 \quad (53)$$

Eq. (53) was obtained by fitting data from $\varrho = 3$ in Fig. 5a and ensuring $F_{i,corr} = 1$ when $F_{iB} = 1$.

The resulting agreement has an error of 4.7% on average, as well as a maximum deviation of 19% (see Fig. 6). We also binned the deviation from Eq. (53) with Re , ϕ and d_i/d_{32} , and found excellent agreement (i.e., absolute deviations between 5% and 7%). It can be noticed that the drag force in case $\varrho = 2$ is significantly deviating from the cases with larger filter sizes. We found that this difference can be entirely attributed to the pressure contribution in Eq. (47), as it is also visible from the different qualitative behavior of the trends as a function of ϱ shown in Fig. 5a and b. This means that a coarse grained cell with $\varrho = 2$ is still affected by local fluctuations of the pressure field. However, in the case of a non-homogeneous system, the resulting drag force \mathbf{f}_i^d calculated according to Eq. (47) will depend on ϱ and the relative position of neighboring particles, so that Eq. (53) will have to take into account sub-grid contributions. This is clearly posing a limit to the grid size in PU-EL since, in case of a non-homogeneous particle distribution, fluid quantities like the velocity field and the pressure gradient may be very different from the homogeneous values used

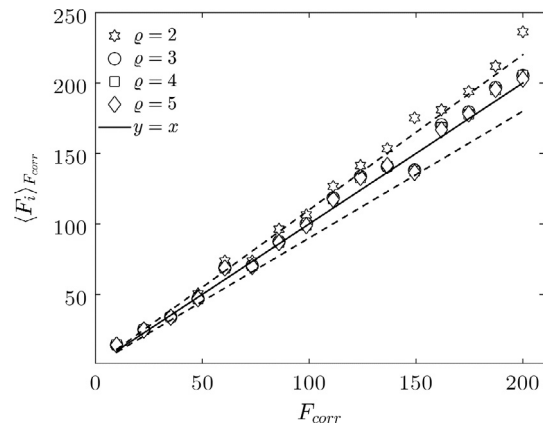


Fig. 6. Parity plot comparing the drag force from the current simulations calculated using Eq. (48) with values predicted by Eq. (53). Dashed lines represent 10% deviation from the closure.

to derive these closures. Thus, specific models for non-homogeneous configurations should be used instead, which are beyond the scope of our present contribution.

We now examine the distribution of the dimensionless per-particle drag force, and consider its scaled standard deviation $\sigma_{F_{corr}}^{F_i}$.

As shown in Fig. 7, we did not observe any significant dependence of $\sigma_{F_{corr}}^{F_i}$ from the mean drag coefficient F_{corr} . This suggests that the relative deviation of F_i from $\langle F_i \rangle_{F_{corr}}$ can be assumed to be approximately constant for the flow regime studied in the present work. Specifically, values of $\sigma_{F_{corr}}^{F_i}$ ranged from 32% to 52% which is generally attributed to the presence of preferred pathways of the flow through the particle array [16]. We note in passing that this is in line with the previous results of Kriebitzsch et al. [14] once their data is rescaled (see the conclusions sections of the present contribution for an in-depth discussion).

The lack of a functional dependence on the mean drag coefficient results in a similar distribution for the relative deviations at different average drag coefficients $\langle F_i \rangle_{F_{corr}}$ (see Fig. 8). In the present work, our data suggests to represent the stochastic fluctuation of the drag force using a modified log normal distribution, i.e. transposed in such a way that the expectation value is zero. This is in contrast to previous work that considered a Gaussian distribution [14], and motivated by the following facts:

- i A log-normal distribution is defined in the range $[0, \infty[$ and, thus, naturally predicts a minimum allowed value for drag coefficient, while the Gauss distribution is defined in $]-\infty, \infty[$ allowing the drag coefficient to assume negative values.
- ii As can be seen from Fig. 8, the distribution of relative deviations is skewed. This is also a consequence of the drag coefficient being lower-bounded.
- iii Our log-normal distribution can be defined using only one parameter (i.e., the standard deviation), which we have demonstrated being a constant within the range of our study. In fact, physically, the minimum allowable value for the relative deviation of -1 (i.e., zero drag force) and the expectation value is, by definition, equal to zero. Thus, this results in a standard log normal distribution with mean value equal to 1.

Clearly, the support of the log normal distribution has to match with that of the drag force relative deviation. This is performed by translating the distribution. Thus, defining the relative deviation $F_{i,\sigma} = (F_i - \langle F_i \rangle_{F_{corr}}) / \langle F_i \rangle_{F_{corr}}$ and the lower bound as $\beta = -1$, the modified log-Normal distribution can be written as:

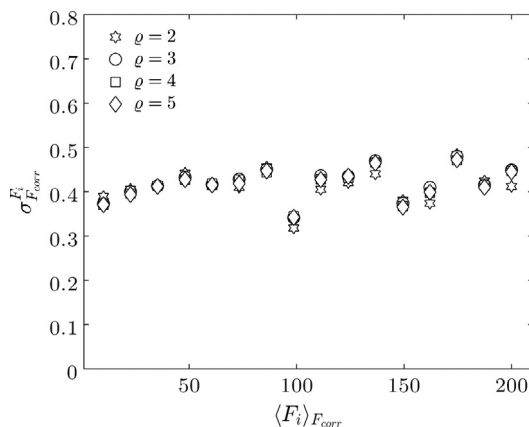


Fig. 7. Scaled standard deviation $\sigma_{F_{corr}}^{F_i}$ over $\langle F_i \rangle_{F_{corr}}$.

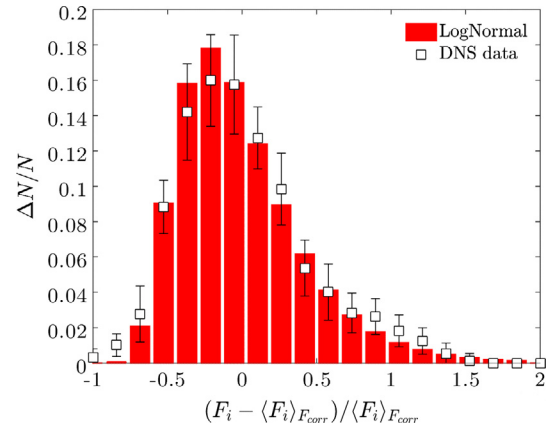


Fig. 8. Number distribution of the relative deviation of the conditionally averaged drag force for different values of F_{corr} . The error bar length corresponds to two standard deviation (i.e., the 68.2% error interval) of the samples in each bin.

$$\mathcal{P}(F_{i,\sigma}) = \frac{1}{(F_{i,\sigma} - \beta)\alpha_F\sqrt{2\pi}} \exp \left\{ -\left[\frac{\ln(F_{i,\sigma} - \beta)}{\sqrt{2}\alpha_F} \right]^2 \right\} \quad (54)$$

As mentioned in item (iii) above, the shape of $\mathcal{P}(F_{i,\sigma})$ is determined by only one parameter (α_F) which turns out to be a constant. By averaging the values of $\sigma_{F_{corr}}^{F_i}$ as they are shown in Fig. 7, we conclude that to a first approximation:

$$\alpha_F \approx 0.416 \quad (55)$$

The choice of a log-normal distribution also allows the stochastic drag coefficient model to be efficiently implemented in PU-EL codes: if ϵ_i is a randomly generated number between 0 and 1, the value of $F_{i,\sigma}$ can be calculated by inverting:

$$\epsilon_i = \int_0^{F_{i,\sigma} - \beta} \mathcal{P}(x) dx \quad (56)$$

where the integral on the right end side is given for a log-normal distribution by:

$$\int_0^{F_{i,\sigma} - \beta} \mathcal{P}(x) dx = \frac{1}{2} + \frac{1}{2} \operatorname{erf} \left[\frac{\ln(F_{i,\sigma} - \beta)}{\sqrt{2}\alpha_F} \right] \quad (57)$$

Which leads to:

$$F_{i,\sigma} = \beta + \exp \left[\operatorname{erf}^{-1}(2\epsilon_i - 1) \sqrt{2}\alpha_F \right] \quad (58)$$

The inverse error function can be obtained using pre-computed lookup tables. In case the coefficients are assumed to be constant (as in our study) the whole expression can be tabulated before starting the computation.

While Eq. (56) can be used to compute the per-particle relative deviations from $\langle F_i \rangle_{F_{corr}}$, the important questions on how this random deviation should be evolved in time remains open. For the time being we note that our model would allow to assign a specific value for $F_{i,\sigma}$ for each particle, and keep this value throughout a PU-EL simulation.

After inverting Eq. (56), the dimensionless drag force acting on a particle i can be computed from:

$$F_i = F_{i,corr}(1 + F_{i,\sigma}) \quad (59)$$

However, it should be noted that in the limit $\phi, Re \rightarrow 0$, the model for the drag force fluctuation is still predicting a drag force between -1 and 2 . Even though a physical interpretation of the above limiting behavior is not as straightforward as one might

think (and lies beyond the scope of our present contribution), it is generally accepted that, in this limit, the resulting drag should return Stokes drag law (i.e., $F_i = 1$).

The proposed model for the drag force fluctuation is able to consistently take this limit into account provided that a suitable expression for the standard deviation α_F is provided. In fact, if all the particles tend to experience the same drag force, it follows that the limit $\phi, Re \rightarrow 0$ implies $\alpha_F \rightarrow 0$, thus making the modified log normal distribution tend to a Dirac delta function. Thus, the future exploration of such a range of parameters (i.e., $\phi, Re \rightarrow 0$) is required in order to obtain a suitable expression for α_F .

Another approach that is less consistent, but perhaps more practical and applicable, consists in calculating the particle-based drag force using the following expression:

$$F_i = 1 + \gamma_F F_{i,corr} \left(1 - \frac{1}{F_{i,corr}} + F_{i,\sigma} \right) \quad (60)$$

where a simple functional form for the unknown function γ_F would be the relation:

$$\gamma_F = \frac{F_{i,corr} - 1}{F_{i,corr}} \quad (61)$$

It is clear that using Definition 61 for γ_F in Eq. (60) enforces the Stokes limit (i.e., $F_{i,corr} \rightarrow 1$), while it approaches the original closure defined in Eq. (59) for large values of $F_{i,corr}$.

As Fig. 8 demonstrates, our proposed model for the drag force fluctuation is able to capture the general trend of the relative drag force deviation reasonably well. However, since we have probed relatively large Reynolds numbers only in the present study, we lack of data that would justify the above presented drag force model for drag coefficients close to unity.

5.3. Nusselt numbers in bidisperse particle beds

The particle-based Nusselt number is defined based on dimensional and dimensionless quantities, respectively, as:

$$Nu_i = \frac{Q_i^*}{\pi d_i \lambda_f (\theta_s^* - \tilde{\theta}_i^*)} = \frac{Q_i Pe}{\pi \eta_i (\theta_s - \tilde{\theta}_i)} \quad (62)$$

In this work, we do not aim on establishing a closure for the bidisperse Nusselt number as a function of the monodisperse one, but we seek for an analogy between heat/mass and momentum transfer. Thus, we will express the bidisperse Nusselt number as a function of the bidisperse drag force, i.e. F_{corr} . There are some advantages in using this approach to formulate a closure model:

- i Existing closures for monodisperse Nusselt numbers are often obtained by flux averaging (in contrast to volume averaging) the temperature field and thus, they have to be corrected using Eq. (17) in order to be applied in coarse-grained models. This operation requires the use of an additional closure and thus, reduces the overall predictive power and range of applicability of the resulting closure model. In addition, we found that scaling the Nusselt number using such closures increases data scattering.
- ii Since closures often require evaluation of long expressions, a simple relation between drag and Nusselt number would be more efficient when implemented in PU-EL or Euler-Euler codes. In most applications (e.g., simulation of heat transfer in fluidized beds) the drag coefficient must be evaluated anyhow, such that a simple relation between drag coefficient and Nusselt number could save computation time.
- iii The range of validity of existing closure models for the Nusselt number (generally $Re \leq 100$ and valid only for monodisperse systems) is outside the range of parameters considered

in our work. Hence, it is not useful to refit parameters in existing correlations, since the functional form for a Nusselt number closure might be fundamentally different.

Since we limited our study to $Pr = 1$, we must assume that the dependence on the Prandtl number is in the form of $Pr^{1/3}$. Thus, the resulting functional form we adapt is:

$$Nu_{i,bi}(Pr, Re, \phi_p, \dots) = Pr^{1/3} G(F_{i,corr}) \quad (63)$$

Thus, any information regarding flow variables or particle population is concealed in F_{corr} and correlated with Nu_{bi} by means of the function G . Indeed, and as shown in Fig. 9, we find a linear relationship of our PR-DNS data for the mean drag coefficient and the Nusselt number. Specifically, we find that

$$Nu_{i,bi} = Pr^{1/3} (12.2 + 0.312 F_{i,corr}) \quad (64)$$

The average deviation of Eq. (64) with respect to our data is 4.6%, with a maximum error of 9.5%.

Examining the distribution of the per-per-particle Nusselt number reveals some interesting finding: again we observed (see Fig. 10) that the scaled standard deviation is approximately constant for the Nusselt number. The standard deviation ranges from approximately 30% to 45%. Following the same approach as for F_{corr} we propose a model for the per-particle Nusselt number based on a log-normally distributed variable as shown in Fig. 11.

Compared to the drag coefficient the log-normal distribution for the Nusselt number is more peaked (i.e., the standard deviation is smaller), and therefore necessitates the use of a α_{Nu} parameter in place of α_F . In order to represent our PR-DNS data reasonably well, the following value for α_{Nu} is recommended:

$$\alpha_{Nu} \approx 0.336 \quad (65)$$

5.4. Global mean Nusselt numbers

We now evaluate the global mean (mixture) Nusselt number which is defined as the Nusselt number that satisfies (with reference to Eq. (21)):

$$Nu_{mix} = \frac{\Lambda Pe}{6 \phi_p} \frac{d_{32}}{d_m} \quad (66)$$

Thus, the above Nusselt number describes the fluid-particle mixture as an homogeneous medium, and is evaluated from a known value for Λ . Notice that we rescaled our Peclet number,

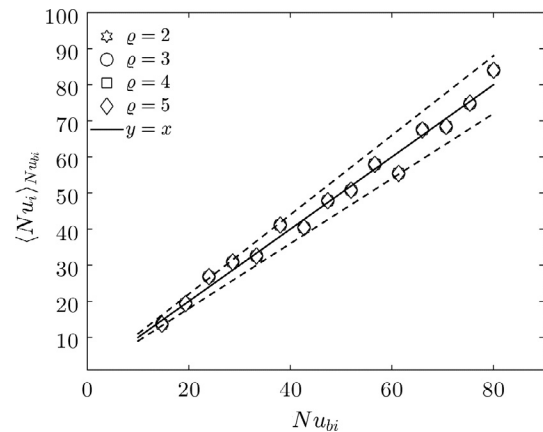


Fig. 9. Parity plot comparing the calculated Nusselt number from the PR-DNS evaluated using Eq. (62) with values predicted using Eq. (64). Dashed lines represent a 10% error corridor.

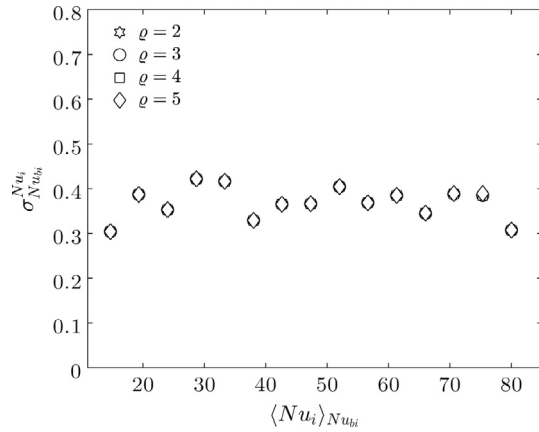


Fig. 10. Scaled standard deviation $\sigma_{Nu_{bi}}^{Nu_i}$ over $\langle Nu_i \rangle_{Nu_{bi}}$. Same as for the drag force F the standard deviation remains approximately constant over the range of mean Nusselt numbers studied.

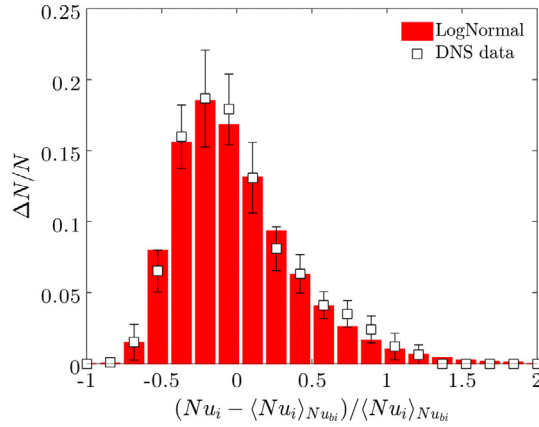


Fig. 11. Number-based distribution of the relative deviation of the conditionally averaged Nusselt number for different values of Nu_{bi} . The error bar length corresponds to two standard deviation (i.e., the 68.2% error interval) of the samples in each bin.

defined using d_m , with the mean Sauter diameter d_{32} . Following the discussion in Section 3, we may express Λ at a certain position $\eta = x/d_m$ as:

$$\Lambda(\eta) = \frac{1}{Pe_L} \left(\frac{Pe_L}{2} - \frac{\ln \Theta(\eta)}{\eta} \right)^2 - \frac{Pe_L}{4} \quad (67)$$

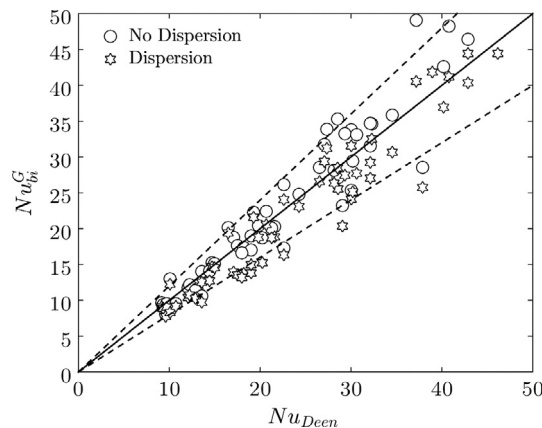


Fig. 12. Parity plot comparing the simulated global Nusselt number Nu_{sim} with the corresponding values from Deen et al. [16]. Dotted lines indicate an error corridor of $\pm 20\%$.

Notice that η should be defined in such a way that $\Theta(\eta) = 1$ at $\eta = 0$ to be consistent with the boundary conditions used in Eq. (25).

In order to evaluate the global mixture Nusselt number, we sampled Θ along the streamwise direction and performed an average over the domain length L :

$$Nu_{bi}^G = \frac{1}{L} \int_0^L Nu_{mix}(\eta) d\eta \approx \frac{1}{N_s} \sum_{i=1}^{N_s} Nu_{mix}(\eta_i) \quad (68)$$

where N_s is the number of samples taken at different equally spaced locations η_i .

Results from this analysis for the case with and without dispersion (i.e., $Pe_L \rightarrow \infty$) are compared with the correlation developed by Deen et al. shown in Fig. 12. Our data suggest that the Nusselt number calculated using this approach (which for the case without dispersion coincides with the approach used by Tavassoli et al. [30]) approaches the value obtained using the closure provided by Deen et al. [16]. The latter closure has been also confirmed by the recent work of Tavassoli et al. [30], highlighting that our results for the mean heat transfer coefficient are in reasonable agreement with results from literature.

6. Conclusions

In the present contribution we studied momentum and heat transport in gas–solid bi-dispersed suspensions. We made use of PR-DNS to derive closures for particle-based quantities and explored the range of usability of models used to describe heat transfer in dense particle beds. Using a simple one-dimensional model for the gas-phase mixture obtained by analytically averaging the thermal transport equations, we derived an expression for a characteristic length scale that characterizes heat (or mass) transfer process in dense homogeneous fluid-particle systems:

$$\lambda_0 = \frac{1}{\sqrt{\frac{Pe_L^2}{4} + Pe_L \Lambda - \frac{Pe_L}{2}}}$$

Furthermore, we applied the idea of a fluid phase saturation length, and showed its relevance for a broad range of Reynolds numbers and particle volume concentrations. We showed that saturation is connected to the λ_0 parameter, and occurs within a few particle diameters in certain situations. The effect of axial dispersion, widely neglected in the literature, was demonstrated to be of major importance.

The problem of saturation is already discussed in literature, however, in a more qualitative way as shown in the work of Teneneti et al. [19], as well as Sun et al. [20]. In our work we have shown that the value of the saturation time and length scale, i.e., (t_{sat} and z_{sat}), may be on the order of a few particle diameters. In such a situation the temperature gradient in the fluid will be extremely high, and the fluid will quickly approach a state of thermal equilibrium with the surrounding particles. It is therefore clear that for small values of z_{sat} the exact value for the Nusselt number is of secondary importance for computing the amount of exchanged heat in a particle bed with length $z < z_{sat}$. Also, in a situation in which z_{sat} is small, the time step required to explicitly evaluate the transferred amount of heat in a PU-EL model will be extremely small. Hence, one would adopt an implicit coupling strategy to ensure stability of the numerical algorithm, at the cost of precision with respect to energy conservation (since implicit coupling cannot ensure identical heat fluxes for both phases). In conclusion we recommend to focus on sufficiently high Peclet number for future studies to quantify the Nusselt number, since these situations are of higher practical interest.

In the present work, we also proposed a modified hybrid fictitious domain-immersed boundary (HFD-IB) method to account for the presence of immersed bodies in non-isothermal flows. This method combines the advantageous convergence properties of a Lagrangian multiplier fictitious domain method with a second order accurate immersed boundary method. The HFD-IB was shown to be accurate, even on relatively coarse grids, in predicting momentum and heat transfer gas in gas-particle system.

The final part of our study applied the HFD-IB to investigate flow through bidisperse beds of spherical particles. We identified that the closure provided by Beetstra et al. [2] for bi-disperse suspensions (which was also shown to be suitable also for tri-disperse suspensions, see [29]) is inaccurate when used in PU-EL-based models. This is because this previous closure does not account for the local mean pressure gradient each particle experiences, but simply accounted for the global pressure gradient in the domain. Since the local mean pressure gradient is known in PU-EL simulations, we proposed a correction to calculate the drag contribution to the total interphase force:

$$F_{i,corr} = -0.1216 + 1.181F_{i,B} + 0.00352F_{i,B}^2$$

The conditionally averaged drag force was shown to agree with this new closure within an average deviation of 4.7%.

We also analyzed the variability of the per-particle drag coefficient, concluding that a log-normal distribution describes this variability reasonably well. This detail is significant, since the recent work of Buist et al. [48] clearly demonstrated that per-particle and mean Nusselt numbers differ (we note in passing that Buist et al. considered the additional complication of a non-uniform particle temperature distribution). Future work might probe whether our proposed model for the per-particle Nusselt number is indeed able to support these findings of Buist et al. [48]. Most important, we showed that the standard deviation relative to the mean drag force is approximately constant over the range of systems studied. This might appear in contrast to previous work [14] on the first view. However, it is important to note that the previous study of Kriebitzsch et al. [14] considered the fluctuation of the total fluid-particle interaction force relative to its mean. This previous study concluded that the fluctuation of the total force decreases with increasing particle concentration. It is now important to consider that (i) the fluctuation of the mean pressure gradient force is weak, as well as (ii) that the pressure gradient increases with increasing particle concentration. Thus, the relative force fluctuations will naturally become smaller with increasing particle concentration, simply because of the larger pressure gradient contribution to the total force. Re-scaling the data in Fig. 13 of Kriebitzsch et al. [14] with $1/(1 - \phi_p)$, i.e., considering the mean drag force as the reference quantity, suggested that fluctuations relative to the drag force are (to a first approximation, and within the scatter of data presented) insensitive to the mean drag force. This is in line with the present contribution, which clearly demonstrated a constant relative drag force variability over a wide range of drag coefficients.

Finally we assessed the existence of a relationship between the average drag force and Nusselt number. Therefore, we first define the Nusselt number (and in particular the coarse-grained temperature) in a way that is consistent with the corresponding coarse-grained model (i.e., a PU-EL model). Hence we do not require additional closures that relate the coarse-grained temperature with a cup-mixing temperature as proposed by Sun et al. [20]. Based on our PR-DNS data we propose the following closure to evaluate the particle-based Nusselt number that relies on the following expression:

$$Nu_{i,bi} = Pr^{1/3}(12.2 + 0.312F_{i,corr}) \quad (69)$$

This closure fits our data with an average deviation of 4.6%, and we show that our results for a global bed-average Nusselt number is in agreement with the recent study of Tavassoli et al. [30]. Again considering the per-particle variability, however this time for the Nusselt number, we again find that a modified log-normal distribution describes this variability reasonably well.

On a final note, we suggest that the expression we provided for $Nu_{i,bi}$ can be modified to return the value corresponding to an isolated particle immersed in a stationary fluid, i.e., $Nu_{i,bi} = 2$ in the limit $\phi, Re \rightarrow 0$. Thus, the particle based Nusselt number can be rewritten (following the same approach used to obtain Eq. (60)) as:

$$Nu_{i,bi} = 2 + Pr^{1/3} \frac{F_{i,corr} - 1}{F_{i,corr}} \left(12.2 - \frac{2}{Pr^{1/3}} + 0.312F_{i,corr} \right) \quad (70)$$

Acknowledgement

The authors acknowledge support from the European Commission through FP7 Grant agreement 604656 (NanoSim), and the NAWI Graz project by providing access to dcluster.tugraz.at. CFDEM is a registered trademark of DCS Computing GmbH. The computational results presented have been achieved (in part) using the Vienna Scientific Cluster (VSC-3).

Appendix A. Verification of the HFD-IB method

In this appendix we demonstrate the correct implementation and the accuracy of the HFD-IB method by comparison with analytic solutions and existing closure in the frame of momentum, heat and mass transfer past one or more spheres.

A.1. Cooling of a sphere immersed in a stationary fluid

We consider the problem of a sphere of diameter d_p immersed in a stationary fluid (i.e., $\mathbf{u} = \mathbf{0}$). We compare the radial temperature profile $T(r, t)$ with the analytical solution for $r > d_p/2$. Due to the symmetry of the problem, the diffusion equation in spherical coordinates can be written as: (see Fig. A.13)

$$\frac{\partial T(r, t)}{\partial t} = \frac{\alpha_f}{r^2} \frac{\partial}{\partial r} \left(r^2 \frac{\partial T(r, t)}{\partial r} \right) \quad (A.1)$$

$$T(r, 0) = 0, \quad T(d_p/2, t) = T_w, \quad T(\infty, t) = T_\infty \quad (A.2)$$

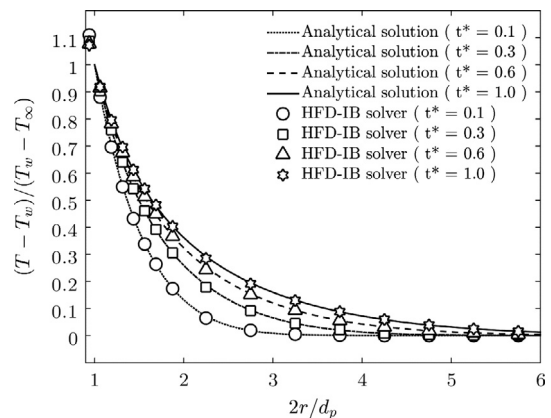


Fig. A.13. Radial temperature field computed using the HFD-IB solver compared with the analytical solution. The maximum error of 0.85% occurs at the surface of the sphere at $t^* = 0.1$. The error quickly decays below 0.4%. Notice that the HFD-IB is imposing a temperature at the boundary cell that is higher than the wall temperature T_w .

where α_f is the heat diffusivity. The well known solution to this problem is:

$$T(r, t) = \frac{1}{r} \left[1 - \operatorname{erf} \left(\frac{r - d_p/2}{2\sqrt{\alpha_f t}} \right) \right] \quad (\text{A.3})$$

We considered a cubic box of $8d_p \times 8d_p \times 8d_p$ with the sphere placed in the center. We used a mesh resolution $h = \Delta x/d_p = 16$ and a dimensionless time step $\Delta t^* = \alpha_f \Delta t/d_p^2 = 10^{-3}$. The solver was found to be in excellent agreement with the analytical solution with an average deviation of 0.2%.

A.2. Forced convection around a sphere

In this test case, transport Eqs. 1a, 1b, and 1c are solved in a cuboid domain containing a single immersed sphere. We used a domain size of $8d_p \times 8d_p \times 16d_p$ and a dimensionless time step $\Delta t = 10^{-4}$. We focused on the local Nusselt number:

$$Nu = \frac{Q^* Re Pr}{\pi(\theta_b - \theta_s)} \quad (\text{A.4})$$

where Q^* is the total interface heat exchange rate calculated using Eq. (35) and θ_b is the dimensionless inlet temperature. We used fixed temperature and velocity boundary condition for the inlet and zero gradient boundary conditions for the remaining boundaries.

Results showed good agreement with closures found in literature, especially with the numerical work from Feng and Michaelides [50]. In addition, Fig. A.14 shows that the Nusselt number is correctly computed (i.e., it is consistent with the existing closure) even for a relatively coarse mesh. The relative error with respect to Feng and Michaelides was found to be less than 1% for $Re < 70$ and increased up to 1.8% at $Re = 100$. We also examined the drag coefficient defined as:

$$C_d = \frac{8f_x^{IB}}{\pi \rho_p d_p^2 U_\infty^2} \quad (\text{A.5})$$

where ρ_p is the particle density, U_∞ is the inlet velocity and f_x^{IB} is the stream-wise component of the dimensionless force acting on the particle calculated using Eq. (36). In Fig. A.15 we plotted the values of C_d obtained for different Reynolds numbers against existing closure. The HFD-IB solver shows good agreement with literature for C_d also with relatively coarse grids. The error was found to be on the order of 4% for $Re = 100$ when using the finest grid and around 5% when the coarsest grid was used.

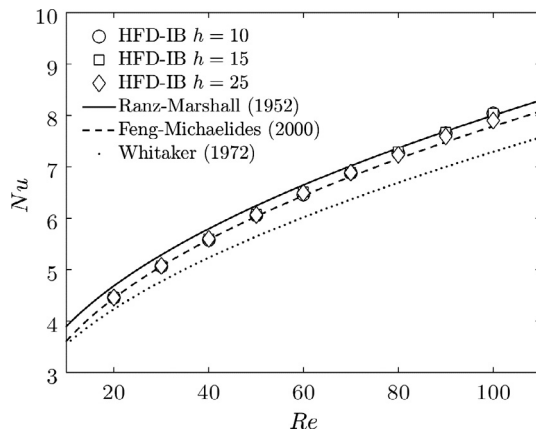


Fig. A.14. Nusselt number calculated using the HFD-IB solver against results found in literature for different Reynolds numbers [49–51]. $h = \Delta x/d_p$ denotes different grid resolutions.

A.3. Creeping flow past a periodic static array of spheres

To simulate flow past a periodic array of spheres, it is sufficient to simulate the flow past a single sphere in a fully periodic box. This test case allows to evaluate the accuracy of the method when two or more particles are close or in contact and thus, to assess the effect of the adaptive order of accuracy for the boundary layer reconstruction. For this case, we solved Eqs. (1a) and (1b) using a body force to drive a flow field with $Re = 2 \cdot 10^{-5}$ in order to ensure a Stokes flow regime. We then compared the dimensionless force defined as:

$$f^* = \frac{f_x^{IB}}{3\pi\mu_f U_0 d_p} \quad (\text{A.6})$$

where μ_f is the dimensionless dynamic viscosity of the fluid (set to $0.2 \text{ kg m}^2/\text{s}$) and U_0 is the imposed dimensionless fluid velocity (set to 10^{-5}). We varied the dimensionless particle diameter d_p to obtain the desired value of ϕ in the periodic box.

The computed values for the dimensionless force (see Table A.2) agree well with the analytical work of Zick and Homsy [54] with a deviation in the range with that obtained by Deen et al. [36]. This may be due to the fact that the forcing term in the immersed boundary they used was also based on a second order interpolation of the fluid variables as was done in the present contribution.

A.4. Forced convection past a chain of three spheres

Finally, we consider the case of forced convection past a chain of three spheres. We compared our results for the particle Nusselt number defined in Eq. (A.4) and for the drag coefficient defined in Eq. (A.5). Same as Ramachandran et al. [55] and Masheshwari et al. [56], we used two different values for the spacing between the three particles, namely $s = 2d_p$ and $4d_p$. Furthermore, contrarily to the case with a single sphere, we used a cylindrical domain of length $16d_p$ or $20d_p$ (depending on the value of s) and radius $5d_p$. The first sphere was centered at a distance $4d_p$ from the inlet. In order to compare with results from Tavassoli et al. [18], we limited the study to a grid resolution of $h = \Delta x/d_p = 15$ (the same grid size he used). We compared the calculated drag coefficient with the one obtained in the work of Maheshwari et al. [56] (Table A.3). It can be seen that the HFD-IB agrees very well, often showing deviations of less than 1% from Mashewari's work. Benchmark for the Nusselt number (Table A.4), shows that the HFD-IB generally agrees with previous works and predicts the Nusselt number experienced by

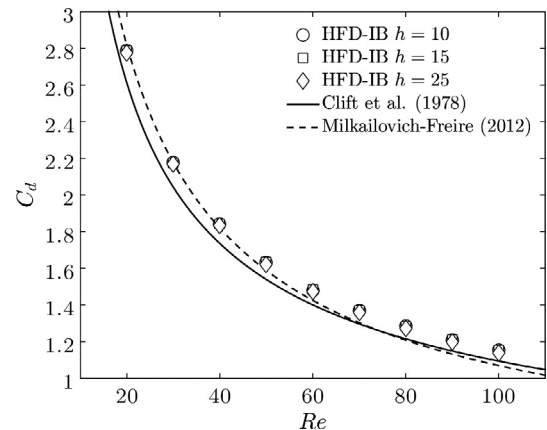


Fig. A.15. Drag coefficient calculated using the HFD-IB solver against results found in literature [52,53] for different Reynolds numbers. $h = \Delta x/d_p$ denotes different grid resolutions.

Table A.2

Deviation from analytical results for the dimensionless drag force. $\Delta f^*/f^*$ represents the deviation from Zick and Homsy [54]. The settings we used are the same as that employed by Deen et al. [36].

ϕ	$d_p/\Delta x$	f^* Zick and Homsy [54]	$\Delta f^*/f^*$ Deen et al. [36] (%)	$\Delta f^*/f^*$ this work (%)
0.5236	32	42.14	1.3	1.1
0.450	30.4	28.1	−2.8	1.4
0.343	27.8	15.4	−1.2	2.7
0.216	23.8	7.442	−0.1	−0.8
0.125	19.9	4.292	−0.7	0.3
0.064	15.9	2.81	−1.3	−1.6
0.027	11.9	2.008	−1.9	−2.8

Table A.3

Drag coefficient experienced by a chain of three spheres. We used *none* to indicate that the deviation is below the precision reported in the work of Maheshwari et al. (two significant digits).

s	Re	C_d deviation from Maheshwari et al.		
		1st (%)	2nd	3rd
2	1	0.8	0.1%	0.2%
2	10	1.0	0.4%	<i>none</i>
2	50	2.0	<i>none</i>	−1.3%
2	100	3.9	<i>none</i>	<i>none</i>
4	1	0.6	−0.8%	−0.6%
4	10	0.9	0.3%	<i>none</i>
4	50	1.9	1.0%	<i>none</i>
4	100	3.7	1.6%	3.5%

Table A.4

Nusselt number in the case of the chain of three spheres.

s	Re	Nu this work			Nu Tavassoli et al.			Nu Ramachandran et al.			Nu Maheshwari et al.		
		1st	2nd	3rd	1st	2nd	3rd	1st	2nd	3rd	1st	2nd	3rd
2	1	2.04	1.54	1.54	2.09	1.58	1.62	2.12	1.81	1.63	2.09	1.83	1.63
2	10	3.31	2.32	2.13	3.45	2.40	2.21	3.37	2.32	2.03	3.32	2.34	2.05
2	50	5.47	3.42	3.10	5.72	3.55	3.19	5.50	3.39	2.98	5.42	3.34	3.08
2	100	7.33	4.24	3.88	–	–	–	7.05	4.18	3.74	6.98	4.23	3.77
4	1	2.23	1.87	1.69	2.31	1.96	1.82	2.17	2.03	1.63	2.20	1.94	1.64
4	10	3.37	2.72	2.53	3.51	2.83	2.62	3.28	2.79	2.49	3.33	2.72	2.53
4	50	5.52	4.05	3.81	5.80	4.21	3.81	5.40	4.18	3.60	5.40	4.11	3.52
4	100	7.13	5.05	4.87	–	–	–	6.96	5.16	4.42	6.91	5.09	4.39

the first sphere with higher accuracy than the method of Tavassoli et al. [18]. This can be understood by noticing that, for a given grid size, the accuracy of the HFD-IB has a weaker dependency on the Reynolds number (see Fig. A.14 in this work and Fig. 6 in the work of Tavassoli et al. [18]).

Appendix B. Particle-based and ensemble averaged drag force

The main focus of this work is to establish correlations for particle-based drag force and Nusselt number, and hence the question arises how to account for the pressure contribution when computing drag forces. In this appendix we show that the standard approach adopted by Beetstra et al. [2] cannot be used to account for the pressure contribution $\mathbf{f}_i^{\nabla p}$.

B.1. Notation and basic definitions

In this appendix we will refer to i as the particle index and to j as the particle class index (referred to particles belonging to class number j , e.g., particles having diameter d_j). Thus, in what follows each particle is characterized by two indexes i and j . Furthermore, we will denote with $\langle \langle * \rangle \rangle_j$ the ensemble average over particles within their particle class, and with $\{ \langle * \rangle \}$ the ensemble average

over all the particle classes. To be more precise, referring to the total force \mathbf{f}_{ji} we define:

$$\langle \mathbf{f} \rangle_j = \frac{1}{N_j} \sum_{i=1}^{N_j} \mathbf{f}_{ji} \quad (\text{B.1})$$

$$\{ \langle \mathbf{f} \rangle \} = \frac{1}{N_{\text{classes}}} \sum_{j=1}^{N_{\text{classes}}} \langle \mathbf{f} \rangle_j \quad (\text{B.2})$$

These averages have to be intended as performed within a configuration, thus an homogeneous distribution of particles experiencing the same global pressure gradient ∇p and characterized by a global particle volume fraction $\phi = \sum_j \phi_j$, a global Reynolds number Re , and number of particles $N_{\text{tot}} = \sum_j N_j$.

We express the total force acting on a single particle using:

$$\mathbf{f}_{j,i} = \mathbf{f}_{j,i}^d + \mathbf{f}_{j,i}^{\nabla p} \quad (\text{B.3})$$

Which is the same as Eq. (46) but now generalized to differentiate between particles in multiple classes. Notice that the index i is not the same as Eq. (46) since in Eq. (B.3) it is conditioned to class j . Furthermore, we account for the pressure term $\mathbf{f}_i^{\nabla p}$ by using:

$$\mathbf{f}_{j,i}^{\nabla p} = \mathbf{f}_j^{\nabla p} = -\frac{\pi}{6} d_j^3 \nabla p = -V_j \nabla p \quad (\text{B.4})$$

Which is the same for particles belonging to the same particle class. Notice that we indicated with V_j the volume of a single particle in class j .

Clearly, the following force balance must hold:

$$N_{tot}\{\mathbf{f}\} = -V\nabla p \quad (\text{B.5})$$

Being V the total volume of the domain (i.e., that of the fluid and all particles).

B.2. Case with one particle class - monodisperse suspensions

Considering the case of just one particle class, the operator $\{(*)\}$ has no effect, and we can drop the index j . Then, substituting Eq. (B.4) into Eq. (B.3) and substituting the resulting pressure gradient into Eq. (B.5) we obtain:

$$\mathbf{f}_i^d = (1 - \phi)\mathbf{f}_i - \phi(\{\mathbf{f}\} - \mathbf{f}_i) \quad (\text{B.6})$$

Which, after application of operator $\langle(*)\rangle_j$, returns the equation used in Beetstra et al. [2] to account for the pressure contribution in the ensemble averaged drag force. However, the additional term $\phi(\{\mathbf{f}\} - \mathbf{f}_i)$ shows that, when extracting statistics for particle-based quantities, the approach of Beetstra et al. [2] cannot be straightforwardly applied, simply because $\mathbf{f}_i^d \neq (1 - \phi)\mathbf{f}_i$. In other words, the pressure term can be regarded as a collective term since it can be indirectly accounted for (i.e., without directly using ∇p) only by considering the average total interphase force in a monodisperse fluid-particle system.

B.3. Case with two particle classes - polydisperse suspensions

If we consider an arbitrary number of particle classes, we find that we cannot account for the individual pressure contribution without considering the globally-averaged drag force $\{\mathbf{f}\}$. Thus, only a relation between globally-averaged quantities can be found:

$$\{\mathbf{f}_d\} = (1 - \phi)\{\mathbf{f}\} \quad (\text{B.7})$$

Furthermore, an equation equivalent to (B.6), but this time based on class-averaged particle forces rather than individual particles, can be obtained:

$$\langle\mathbf{f}_d\rangle_j = \left(1 - \phi_j \frac{N_{tot}}{N_j}\right)\langle\mathbf{f}\rangle_j - \phi_j \frac{N_{tot}}{N_j}(\{\mathbf{f}_d\} - \langle\mathbf{f}\rangle_j) \quad (\text{B.8})$$

This equation returns Eq. (B.7) when averaged over all the particle classes. Notice that these equations imply $\langle\mathbf{f}_d\rangle_j \neq (1 - \phi)\langle\mathbf{f}\rangle_j$, which is the approach used by Beetstra et al. [2]. Also other expressions like $\langle\mathbf{f}_d\rangle_j = (1 - \phi_j)\langle\mathbf{f}\rangle_j$ are clearly erroneous. The reason can

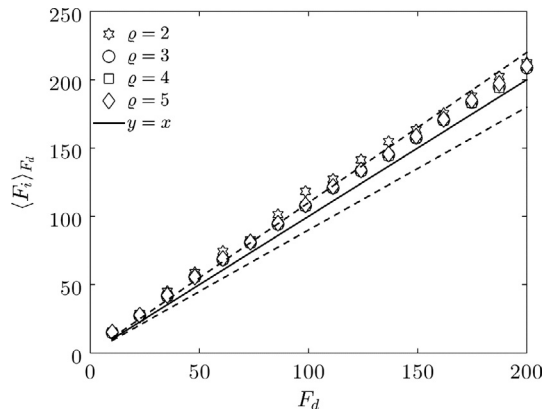


Fig. B.16. Parity plot comparing the dimensionless drag force from the current simulations (i.e., F_i) calculated using Eq. (48), with predictions based on Eq. (B.9) (i.e., F_d) that rely on the closure of Beetstra et al. The dashed lines represent a 10% error corridor.

be found by examining Eq. (B.5). The global balance implies that the pressure gradient is connected with the sum of all interphase forces and thus, cannot be expressed as a function of just one subset (i.e., one particle or one particle class) of the fluid-particle system.

B.4. Application to the current case

The approach used in the current study (i.e., that presented in Section 5) is consistent with the above considerations. Specifically, we show that using the Favre averaged pressure gradient is in agreement with the following equation:

$$\mathbf{f}_{j,i}^d = \mathbf{f}_{j,i} - \phi_j \frac{N_{tot}}{N_j}\{\mathbf{f}\} \quad (\text{B.9})$$

Which can be obtained straightforwardly by substituting Eq. (B.4) into (B.3) and finally into (B.5). If Eq. (B.9) is satisfied in our simulations, then our approach is consistent. The term N_{tot}/N_j is, for a bidisperse system, given by from ϕ_m/ϕ_M :

$$N_{tot}/N_j = \left(1 + \frac{d_j^2}{d_k^2} \frac{\phi_k}{\phi_j}\right) \quad k, j = 1, 2 \quad k \neq j \quad (\text{B.10})$$

The term $\{\mathbf{f}\}$ is typically not reported in literature (also not by Beetstra et al.). However, one may use the drag from Beetstra et al. [2] (i.e., as defined in Eq. (49)) and consider (the incorrect) Eq. (52) to backup the total interaction force implied by Beetstra et al.:

$$\{\mathbf{f}\} = \frac{N_1 d_1 F_{B,1} + N_2 d_2 F_{B,2}}{N_{tot}(1 - \phi)} \quad (\text{B.11})$$

where 1, 2 refer to the two particle classes considered here.

Fig. B.16 shows that Eq. (B.9) slightly underpredicts the drag force from our simulation but still agrees within 10% for filter sizes $\rho > 2$. This deviation can be interpreted as the true difference between our simulation results and the one of Beetstra et al. after applying the same correction for the pressure gradient.

References

- [1] F. Municchi, C. Goniva, S. Radl, Highly efficient spatial data filtering in parallel using the opensource library CPPPO, *Comput. Phys. Commun.* 207 (2016) 400–414, <http://dx.doi.org/10.1016/j.cpc.2016.05.026>, URL <<http://linkinghub.elsevier.com/retrieve/pii/S0010465516301606>>.
- [2] R. Beetstra, Drag force of intermediate Reynolds number flow past mono- and bidisperse arrays of spheres, *IFAC Proc. Vol. (IFAC-PapersOnline)* 7 (2) (2009) 405–410, <http://dx.doi.org/10.1002/aic>.
- [3] T.B. Anderson, R.O.Y. Jackson, A fluid mechanical description of fluidized beds, *Ind. Eng. Chem. Fundamen.* 6 (4) (1967) 527–539.
- [4] G. Kelbaliyev, K. Ceylan, A theoretical model for the particle distribution in a polydispersed solid mixture under hydrodynamic and gravitational effects, *Powder Technol.* 115 (1) (2001) 84–89, [http://dx.doi.org/10.1016/S0032-5910\(00\)00281-3](http://dx.doi.org/10.1016/S0032-5910(00)00281-3), URL <<http://linkinghub.elsevier.com/retrieve/pii/S0032591000002813>>.
- [5] M.a.V.D. Hoef, R. Beetstra, J.A.M. Kuipers, Lattice-Boltzmann simulations of low-Reynolds-number flow past mono- and bidisperse arrays of spheres: results for the permeability and drag force, *J. Fluid Mech.* 528 (2005) 233–254, <http://dx.doi.org/10.1017/S00222112004003295>, URL <http://www.journals.cambridge.org/abstract_S00222112004003295>.
- [6] G. Tryggvason, S. Thomas, J. Lu, B. Aboulhasanzadeh, Multiscale issues in DNS of multiphase flows, *Acta Math. Sci.* (2) (2010) 551–562.
- [7] Sankaran Sundaresan, Stefan Radl, Christian C. Milioli, Fernando E. Milioli, Coarse-grained models for momentum, energy and species transport in gas-particle flows, in: *The 14th International Conference on Fluidization From Fundamentals to Products*, 2013.
- [8] S. Radl, S. Sundaresan, A drag model for filtered Euler Lagrange simulations of clustered gas particle suspensions, *Chem. Eng. Sci.* 117 (2014) 416–425, <http://dx.doi.org/10.1016/j.ces.2014.07.011>.
- [9] M. Ye, M.A. Van Der Hoef, J.A.M. Kuipers, A numerical study of fluidization behavior of Geldart A particles using a discrete particle model, *Powder Technol.* 139 (2) (2004) 129–139, <http://dx.doi.org/10.1016/j.powtec.2003.10.012>.
- [10] J. Capecelatro, O. Desjardins, An Euler-Lagrange strategy for simulating particle-laden flows, *J. Comput. Phys.* 238 (2013) 1–31, <http://dx.doi.org/10.1016/j.jcp.2012.12.015>.

- [11] J. Capecelatro, O. Desjardins, An Euler-Lagrange strategy for simulating particle-laden flows, *J. Comput. Phys.* 238 (2013) 1–31, <http://dx.doi.org/10.1016/j.jcp.2012.12.015>.
- [12] J. Capecelatro, O. Desjardins, R.O. Fox, Numerical study of collisional particle dynamics in cluster-induced turbulence, *J. Fluid Mech.* 747 (2014) R2, <http://dx.doi.org/10.1017/jfm.2014.194>, URL <http://www.journals.cambridge.org/abstract_S0022112014001943>.
- [13] J. Capecelatro, O. Desjardins, R.O. Fox, On fluid-particle dynamics in fully developed cluster-induced turbulence, *J. Fluid Mech.* 780 (2015) 578–635, <http://dx.doi.org/10.1017/jfm.2015.459>, URL <http://www.journals.cambridge.org/abstract_S0022112015004590>.
- [14] S.H.L. Kriebitzsch, M.A.V.D. Hoef, J.A.M. Kuipers, Drag force in discrete particle models continuum scale or single particle scale?, *AIChE J.* (59) (2012) 316–324, <http://dx.doi.org/10.1002/aic>.
- [15] W. Holloway, S. Benyahia, C.M. Hrenya, S. Sundaresan, Meso-scale structures of bidisperse mixtures of particles fluidized by a gas, *Chem. Eng. Sci.* 66 (19) (2011) 4403–4420, <http://dx.doi.org/10.1016/j.ces.2011.05.037>.
- [16] N.G. Deen, E.A.J.F. Peters, J.T. Padding, J.A.M. Kuipers, Review of direct numerical simulation of fluid-particle mass, momentum and heat transfer in dense gas-solid flows, *Chem. Eng. Sci.* 116 (2014) 710–724, <http://dx.doi.org/10.1016/j.ces.2014.05.039>.
- [17] J. Derksen, Simulations of solid liquid mass transfer in fixed and fluidized beds, *Chem. Eng. J.* 255 (2014) 233–244, <http://dx.doi.org/10.1016/j.cej.2014.06.067>, URL <<http://linkinghub.elsevier.com/retrieve/pii/S1385894714007980>>.
- [18] H. Tavassoli, S. Kriebitzsch, M. van der Hoef, E. Peters, J. Kuipers, Direct numerical simulation of particulate flow with heat transfer, *Int. J. Multiph. Flow* 57 (2013) 29–37, <http://dx.doi.org/10.1016/j.ijmultiphaseflow.2013.06.009>, URL <<http://linkinghub.elsevier.com/retrieve/pii/S0301932213001055>>.
- [19] S. Tenneti, B. Sun, R. Garg, S. Subramaniam, Role of fluid heating in dense gas-solid flow as revealed by particle-resolved direct numerical simulation, *Int. J. Heat Mass Transf.* 58 (1–2) (2013) 471–479, <http://dx.doi.org/10.1016/j.ijheatmasstransfer.2012.11.006>.
- [20] B. Sun, S. Tenneti, S. Subramaniam, Modeling average gas solid heat transfer using particle-resolved direct numerical simulation, *Int. J. Heat Mass Transf.* 86 (2015) 898–913, <http://dx.doi.org/10.1016/j.ijheatmasstransfer.2015.03.046>, URL <<http://linkinghub.elsevier.com/retrieve/pii/S001793101500304X>>.
- [21] A.T. Andrews IV, P.N. Loezos, S. Sundaresan, Coarse-grid simulation of gas-particle flows in vertical risers, *Ind. Eng. Chem. Res.* 44 (16) (2005) 6022–6037, <http://dx.doi.org/10.1021/ie0492193>.
- [22] F.B. Usabiaga, I. Pagonabarraga, R. Delgado-Buscalioni, Inertial coupling for point particle fluctuating hydrodynamics, *J. Comput. Phys.* 235 (2013) 701–722, <http://dx.doi.org/10.1016/j.jcp.2012.10.045>.
- [23] C. Peskin, Flow patterns around heart valves: a numerical method, *J. Comput. Phys.* 10 (2) (1972) 252–271, [http://dx.doi.org/10.1016/0021-9991\(72\)90065-4](http://dx.doi.org/10.1016/0021-9991(72)90065-4).
- [24] S.S. Smagulov, Fictitious Domains Method for Navier-Stokes Equations, Preprint CC SA USSR 68.
- [25] A.J. Sierakowski, A. Prosperetti, Resolved-particle simulation by the Physalis method: enhancements and new capabilities, *J. Comput. Phys.* 309 (2016) 164–184, <http://dx.doi.org/10.1016/j.jcp.2015.12.057>.
- [26] F. Auricchio, D. Boffi, L. Gastaldi, A. Lefieux, A. Reali, On a fictitious domain method with distributed Lagrange multiplier for interface problems, *Appl. Numer. Math.* 95 (2015) 36–50, <http://dx.doi.org/10.1016/j.apnum.2014.05.013>, URL <<http://linkinghub.elsevier.com/retrieve/pii/S0168927414001238>>.
- [27] A. Wachs, A. Hammouti, G. Vinay, M. Rahmani, Accuracy of finite volume/staggered grid distributed Lagrange multiplier/fictitious domain simulations of particulate flows, *Comput. Fluids* 115 (2015) 154–172, <http://dx.doi.org/10.1016/j.compfluid.2015.04.006>, URL <<http://linkinghub.elsevier.com/retrieve/pii/S0045793015001152>>.
- [28] D. Geldart, J. Baeyens, D. Pope, P. Van De Wijer, Segregation in beds of large particles at high velocities, *Powder Technol.* 30 (1981) 195–205, [http://dx.doi.org/10.1016/0032-5910\(81\)80012-5](http://dx.doi.org/10.1016/0032-5910(81)80012-5).
- [29] W. Holloway, X. Yin, S. Sundaresan, Fluid-particle drag in inertial polydisperse gas solid suspensions, *AIChE J.* 57 (11) (2011) 3199–3209, <http://dx.doi.org/10.1002/aic>.
- [30] H. Tavassoli, E. Peters, J. Kuipers, Direct numerical simulation of non-isothermal flow through dense bidisperse random arrays of spheres, *Powder Technol.* <http://dx.doi.org/10.1016/j.powtec.2016.09.088>, URL <<http://linkinghub.elsevier.com/retrieve/pii/S00325910160306684>>.
- [31] J.J. Wylie, D.L. Koch, A.J.C. Ladd, Rheology of suspensions with high particle inertia and moderate fluid inertia, *J. Fluid Mech.* 480 (2003) 95–118, <http://dx.doi.org/10.1017/S0022112002003531>, URL <http://www.journals.cambridge.org/abstract_S0022112002003531>.
- [32] C. Kloss, C. Goniva, A. Hager, S. Amberger, S. Pirker, Models, algorithms and validation for opensource DEM and CFD-DEM, *Prog. Comput. Fluid Dyn.* 12 (2012) 140–152, <http://dx.doi.org/10.1504/PCFD.2012.047457>.
- [33] W. Holloway, S. Sundaresan, Filtered models for bidisperse gas-particle flows, *Chem. Eng. Sci.* 108 (2014) 67–86, <http://dx.doi.org/10.1016/j.ces.2013.12.037>, Available from: <1204.6053v1> URL <<http://dx.doi.org/10.1016/j.ces.2012.07.019>>.
- [34] R.J. Hill, D.L. Koch, A.J.C. Ladd, The first effects of fluid inertia on flows in ordered and random arrays of spheres, *J. Fluid Mech.* 448 (2001) 243–278, <http://dx.doi.org/10.1017/S0022112001005948>.
- [35] D. Gunn, Transfer of heat or mass to particles in fixed and fluidised beds, *Int. J. Heat Mass Transf.* 21 (4) (1978) 467–476, [http://dx.doi.org/10.1016/0017-9310\(78\)90080-7](http://dx.doi.org/10.1016/0017-9310(78)90080-7), URL <<http://www.sciencedirect.com/science/article/pii/0017931078900807>>.
- [36] N.G. Deen, S.H.L. Kriebitzsch, M.A. van der Hoef, J.A.M. Kuipers, Direct numerical simulation of flow and heat transfer in dense fluid-particle systems, *Chem. Eng. Sci.* 81 (2012) 329–344, <http://dx.doi.org/10.1016/j.ces.2012.06.055>.
- [37] J.M.P.Q. Delgado, A critical review of dispersion in packed beds, *Heat Mass Transf./Waerme- und Stoffuebertragung* 42 (4) (2006) 279–310, <http://dx.doi.org/10.1007/s00231-005-0019-0>.
- [38] P. Angot, A unified fictitious domain model for general embedded boundary conditions, *C.R. Math.* 341 (11) (2005) 683–688, <http://dx.doi.org/10.1016/j.crma.2005.09.046>.
- [39] R. Glowinski, T. Pan, T. Hesla, D. Joseph, J. Périaux, A fictitious domain approach to the direct numerical simulation of incompressible viscous flow past moving rigid bodies: application to particulate flow, *J. Comput. Phys.* 169 (2) (2001) 363–426, <http://dx.doi.org/10.1006/jcp.2000.6542>, URL <<http://linkinghub.elsevier.com/retrieve/pii/S00219991100965422>>.
- [40] L. Zhang, K. Liu, C. You, Fictitious domain method for fully resolved reacting gas solid flow simulation, *J. Comput. Phys.* 299 (2015) 215–228, <http://dx.doi.org/10.1016/j.jcp.2015.07.010>, URL <<http://linkinghub.elsevier.com/retrieve/pii/S0021999115004556>>.
- [41] M. Uhlmann, An immersed boundary method with direct forcing for the simulation of particulate flows, *J. Comput. Phys.* 209 (2) (2005) 448–476, <http://dx.doi.org/10.1016/j.jcp.2005.03.017>.
- [42] F. Sabetghadam, Exact Imposition of the Regular Rigid Immersed Surfaces on the Solution of the Incompressible Navier Stokes Equations. 10.13140/RG.2.1.4800.4001. Available from: <1412.5130>.
- [43] Z.-G. Feng, E.E. Michaelides, Heat transfer in particulate flows with direct numerical simulation (DNS), *Int. J. Heat Mass Transf.* 52 (3–4) (2009) 777–786, <http://dx.doi.org/10.1016/j.ijheatmasstransfer.2008.07.023>, URL <<http://linkinghub.elsevier.com/retrieve/pii/S0017931008004249>>.
- [44] A. Gilmanov, F. Sotiropoulos, A hybrid Cartesian/immersed boundary method for simulating flows with 3D, geometrically complex, moving bodies, *J. Comput. Phys.* 207 (2) (2005) 457–492, <http://dx.doi.org/10.1016/j.jcp.2005.01.020>.
- [45] A. Mark, B.G. van Wachem, Derivation and validation of a novel implicit second-order accurate immersed boundary method, *J. Comput. Phys.* 227 (13) (2008) 6660–6680, <http://dx.doi.org/10.1016/j.jcp.2008.03.031>, URL <<http://linkinghub.elsevier.com/retrieve/pii/S0021999108001770>>.
- [46] A. Mark, R. Rundqvist, F. Edelvik, Comparison between different immersed boundary conditions for simulation of complex fluid flows, *Fluid Dyn. Mater. Process.* 7 (3) (2011) 241–258.
- [47] B. Blais, M. Lassaingne, C. Goniva, L. Fradette, A semi-implicit immersed boundary method and its application to viscous mixing, *Comput. Chem. Eng.* 85 (2016) 136–146.
- [48] K. Buist, B. Backx, N. Deen, J. Kuipers, A combined experimental and simulation study of fluid-particle heat transfer in dense arrays of stationary particles, *Chem. Eng. Sci.* (2016) 1–11, <http://dx.doi.org/10.1016/j.ces.2016.04.022>, URL <<http://linkinghub.elsevier.com/retrieve/pii/S0009250916301853>>.
- [49] W. Ranz, W. Marshal, Evaporation from drops, *Chem. Eng. Prog.* (48) (1952) 141–146.
- [50] Z.-G. Feng, E.E. Michaelides, A numerical study on the transient heat transfer from a sphere at high Reynolds and Peclet numbers, *Int. J. Heat Mass Transf.* 43 (2) (2000) 219–229, [http://dx.doi.org/10.1016/S0017-9310\(99\)00133-7](http://dx.doi.org/10.1016/S0017-9310(99)00133-7).
- [51] S. Whitaker, Forced convection heat transfer correlations for flow in pipes, past flat plates, single, *AIChE J.* 18 (2) (1972) 361–371.
- [52] M. Clift, R. Grace, J.R. Weber, Bubbles, Drops and Particles, vol. 94, 1978, <http://dx.doi.org/10.1017/S0022112079221290>, URL <http://www.journals.cambridge.org/abstract_S0022112079221290>.
- [53] M. Mikhailov, a.S. Freire, The drag coefficient of a sphere: an approximation using Shanks transform, *Powder Technol.* 237 (2013) 432–435, <http://dx.doi.org/10.1016/j.powtec.2012.12.033>, URL <<http://linkinghub.elsevier.com/retrieve/pii/S0032591012008327>>.
- [54] A.A. Zick, G.M. Homsy, Stokes flow through periodic arrays of spheres, *J. Fluid Mech.* 2 (2) (1982), 115.
- [55] R.S. Ramachandran, C. Kleinstreuer, T. Wang, Forced convection heat transfer of interacting spheres, *Numer. Heat Transf. Part A: Appl.* 15 (4) (1989) 471–487.
- [56] A. Maheshwari, R.P. Chhabra, G. Biswas, Effect of blockage on drag and heat transfer from a single sphere and an in-line array of three spheres, *Powder Technol.* 168 (2) (2006) 74–83, <http://dx.doi.org/10.1016/j.powtec.2006.07.007>.